SPS ANTENNA POINTING CONTROL

Prepared for

National Adronautics and Space Administration
George C. Marshall Space Flight Center
Marshall Space Flight Center, Alabama 35812

by

The University of Tennessee
Electrical Engineering Department
Systems and Radar Laboratory
Knoxville, Tennessee 37916

Under Contract NAS8-33604

Principal Investigator
James C. Hung

N80-24515

(NASA-CR-161446) SPS ANTENNA POINTING
CONTROL (Tennessee Univ.) 84 p CSCL 13I
HC A05/MF A01

Unclas
G3/32 20976

29 February 1980

ACKNOWLEDGMENT

This report documents the work done under contract NAS8-33604 which was sponsored by the National Aeronautics and Space Administration (NASA), Marshall Space Flight Center (MSFC). The work was performed during the period from 1 August 1979 to 29 February 1980.

Dr. P. Z. Peebles was responsible for the task concerning the pointing error sensing method, while Drs. J. C. Hung and C. W. Lee were jointly responsible for tasks involving the rigid body pointing control and the modeling approaches for the flexible collector. The Contracting Officer's Technical Representative at NASA/MSFC was Mr. J. T. Howell.

Table of Contents

Appendices

List of Figures

1. INTRODUCTION

This report documents the results of a six-month study on the pointing control of a microwave antenna of the Satellite Power System (SPS). The study, performed under NASA contract NAS8-33604, may be considered as the continuation of an early effort on the accuracy analysis of pointing control system of SPS, which was conducted under NASA contract NAS8-33065. Primary goals of the study encompass three areas, namely, the SPS antenna pointing error sensing method, a rigid body pointing control design study, and approaches for modeling the flexible body characteristics of the solar collector.

Accuracy requirements for the antenna pointing control consist of a mechanical pointing control accuracy of three (3) arc-minutes and an electronic phased array pointing accuracy of three (3) arc-seconds. Results of the study, based on the factors considered in current analysis, show that the three arc-minute overall pointing control accuracy can be achieved in practice.

Section 2 of this report deals with the antenna pointing error sensing method and its performance. Among the topics discussed are the pointing error sensing method, received signals, subarray signal processing, array signal processing, effect of noise, and effect of vibrations.

Section 3 presents the details of a mechanical pointing control design for the antenna. Included in the section are the baseline satellite configuration and a set of baseline parameters, an estimation of motor rating and motor parameters, slip-ring friction characteristics, the effect of centrifugal force-induced torque on antenna due to gimbal rotation, the effect of variation of antenna moment of inertia due to its changing attitude, control system modeling, control system design, system simulation, and the effect of noise in sensed pointing error signal. Also included in the section is the effect of collector vibration on the accuracy of pointing control.

Shortly after the start of the study, it was found that the required effort for an analytical modeling of the flexible structure of the solar collector was immense, way beyond the planned effort. As a result, work in this area was redirected into two directions. The first direction is to explore the approaches for obtaining an analytic flexible model, and the second direction is to estimate the effect of the collector's flexible body vibration on the antenna pointing control accuracy. Section 3 is devoted to the discussion of the approaches for the flexible collector modeling.

A list of references and two appendices are included for the convenience of readers.

2. ERROR SENSING METHOD FOR ANTENNA POINTING

In the final report of an earlier effort [1] a method was proposed for developing angle error signals to be used by angle servomechanisms to point the antenna toward the ground station. In this effort, the proposed method has been shown to be feasible. In addition, a normalization technique, similar to that used in angle tracking radar, has been added that produces error signals that are independent of received signal magnitude. Finally, some results related to affects of vibration and noise have been derived.

2.1 Sensing Method

The basic concept is illustrated in Figure 1. Two intersecting linear arrays formed from subarrays of the main array are used to develop error signals. The array normal to axis 1 is used to develop an error signal proportional to the error that the antenna pointing direction makes relative to the desired direction (toward the earth site) in a plane for which axis 1 is normal (error about axis 1). The other array generates a signal proportional to the (space) orthogonal angle in the plane for which axis 2 is normal. The two error signals are used by angle servomechanisms to turn the antenna about axes 1 and 2 to cause the errors to approach zero.

Each array is presumed to have $2N + 1 = M$ subarrays with the common subarray at the antenna's center serving as the "reference" for the two arrays. In general, the two arrays do not have to have equal numbers of subarrays; however, since accuracy requirements are likely to be the same in both coordinates, there seems to be no reason to not make the two identical, as is assumed in following discussions.

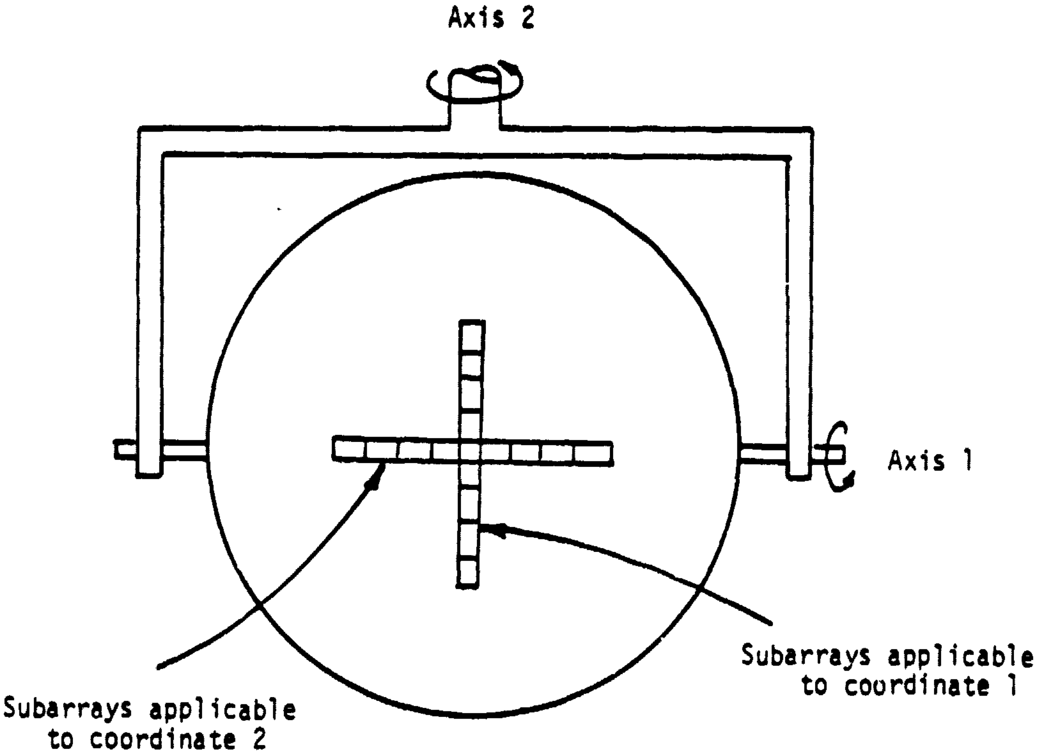

Figure 1. Subarrays applicable to gimbal servo error generation.

2.2 Received Signals

We define antenna-centered coordinates as shown in Figure 2 where x and y are axes in the plane of the antenna's face. Axis z is the antenna's true pointing direction. A wave arriving from the earth site makes an angle θ from the z (boresight axis) direction; it has an "orientation" defined by an angle ϕ in the xy plane. Using these definitions we find the signal received by a typical subarray located along the x direction. Only the x axis array is analyzed since the other behaves in a similar manner.

The error angles sensed by the system in Figure 2 are θ_x (in the xz plane) and θ_y (in the yz plane). The various angles are related by

$$\tan(\theta_x) = \tan(\theta) \cos(\phi) \qquad (1)$$

$$\tan(\theta_y) = \tan(\theta) \sin(\phi) \qquad (2)$$

from geometry.

A typical subarray pattern in the SPS system will have a uniform illumination function, have a rectangular shape (side-lengths X and Y) and a one-way voltage pattern, denoted $G(\theta.\phi)$ by

$$G(\theta,\phi) = \mathrm{Sa}\left[\frac{\pi X}{\lambda} \sin(\theta)\cos(\phi)\right]\mathrm{Sa}\left[\frac{\pi Y}{\lambda} \sin(\theta)\sin(\phi)\right] \qquad (3)$$

where

$$\mathrm{Sa}(\xi) = \frac{\sin(\xi)}{\xi} \qquad (4)$$

and λ is wavelenght. If we now recognize that $|\theta|<<1$ for any reasonable SPS system, then $|\theta_x|<<1$ and $|\theta_y|<<1$, so (1) through (3) give

$$\theta_x \approx \theta \cos(\phi) \qquad (5)$$

$$\theta_y \approx \theta \sin \phi \qquad (6)$$

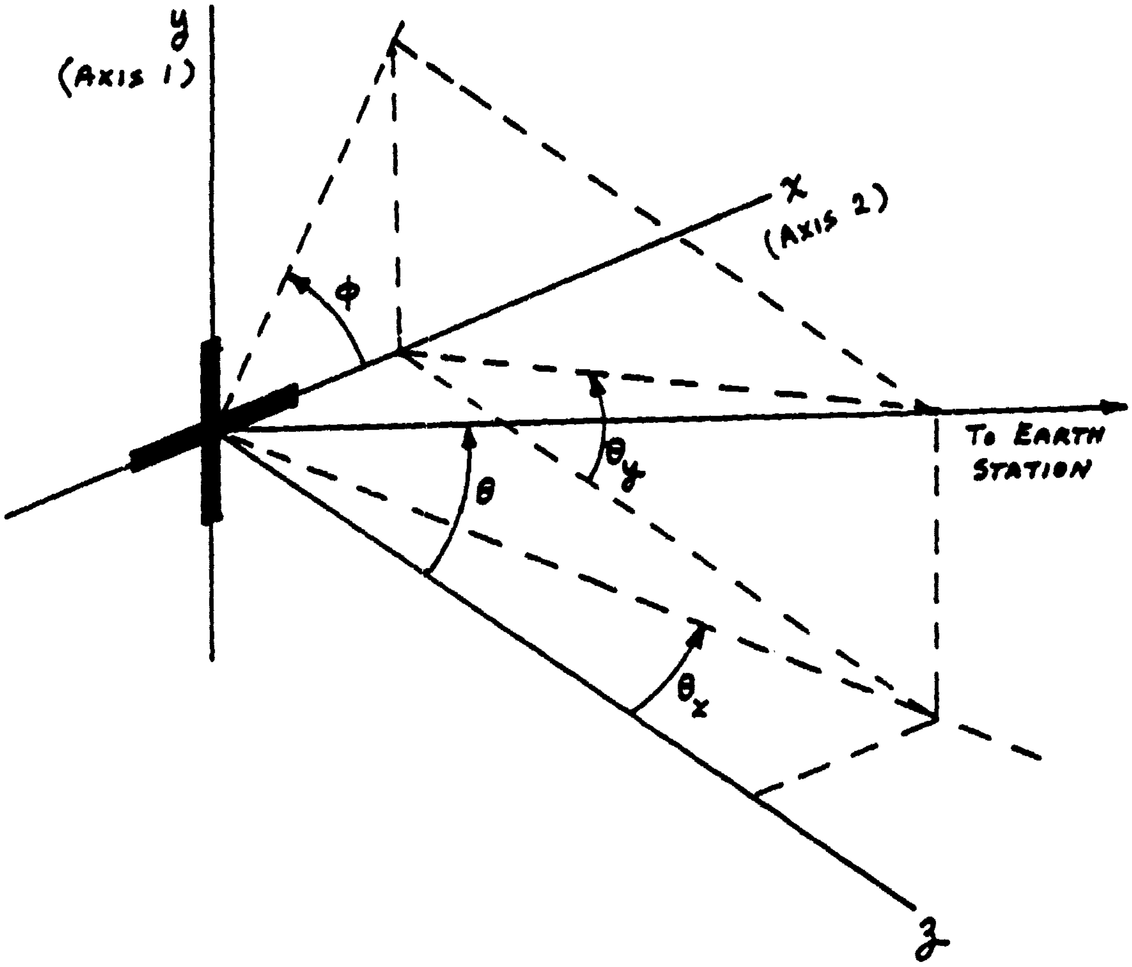

Figure 2. Antenna-centered coordinates.

$$G(\theta,\phi) \approx Sa[(\pi X/\lambda)\theta\cos(\phi)]\, Sa[(\pi Y/\lambda)\theta\sin(\phi)]$$

$$= Sa[\pi X\theta_x/\lambda] Sa[\pi Y\theta_y/\lambda] = G(\theta_x,\theta_y) \qquad (7)$$

Now consider the array of subarrays along the x axis as shown in Figure 3. Subarray locations along x are nX, $-N \leq n \leq N$, and they have displacement in the z direction of z_n and tilt angles θ_{xn} (tilt in the other coordinate is θ_{yn}). If v_n denotes the voltage produced by the nth subarray by a wave having error angles θ_x and θ_y, then

$$v_n = A_0\, G(\theta_x+\theta_{xn},\ \theta_y+\theta_{yn})\cos[\phi_{pilot} + \frac{2\pi nX}{\lambda}\sin(\theta_x) + \frac{2\pi z_n}{\lambda}\cos(\theta_x)] \qquad (8)$$

where A_0 is the voltage produced when the subarray points toward the pilot source without tilt error and ϕ_{pilot} is the phase of the arriving pilot signal at the reference (n=0) subarray. Since $|\theta_x| \ll 1$,

$$v_n \approx A_0\, G(\theta_x+\theta_{xn},\ \theta_y+\theta_{yn})\cos[\phi_{pilot} + \frac{2\pi nX\theta_x}{\lambda} + \frac{2\pi z_n}{\lambda}]. \qquad (9)$$

2.3 Subarray Signal Processing

We next show that desirable error sensing occurs if the signal processing of Figure 4(a) is available at each subarray in the line array. Straightforward analysis gives

$$\left.\begin{matrix} e_n^{(+)} \\ e_n^{(-)} \end{matrix}\right\} = \frac{A_0}{2}\, G(\theta_x+\theta_{xn},\ \theta_y+\theta_{yn})\ \{\cos[\frac{2\pi nX\theta_x}{\lambda} + \frac{2\pi(z_n-z_0)}{\lambda} + n\theta_q]$$

$$\pm\cos[\frac{2\pi nX\theta_x}{\lambda} + \frac{2\pi(z_n-z_0)}{\lambda} - n\theta_q]\}. \qquad (10)$$

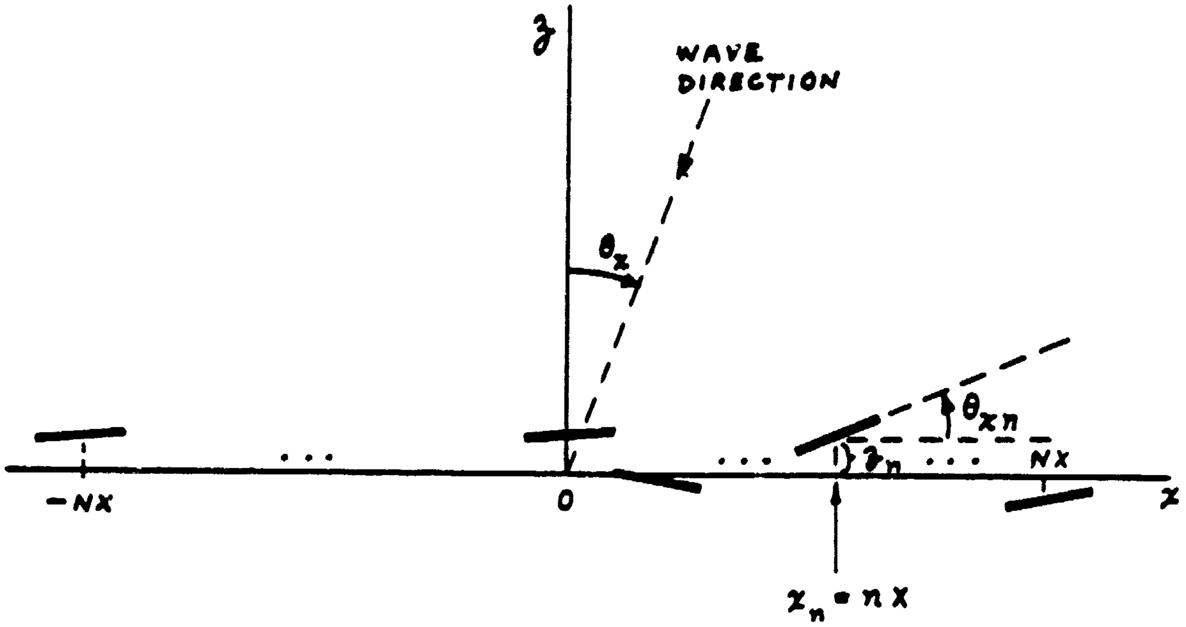

Figure 3. Subarray locations.

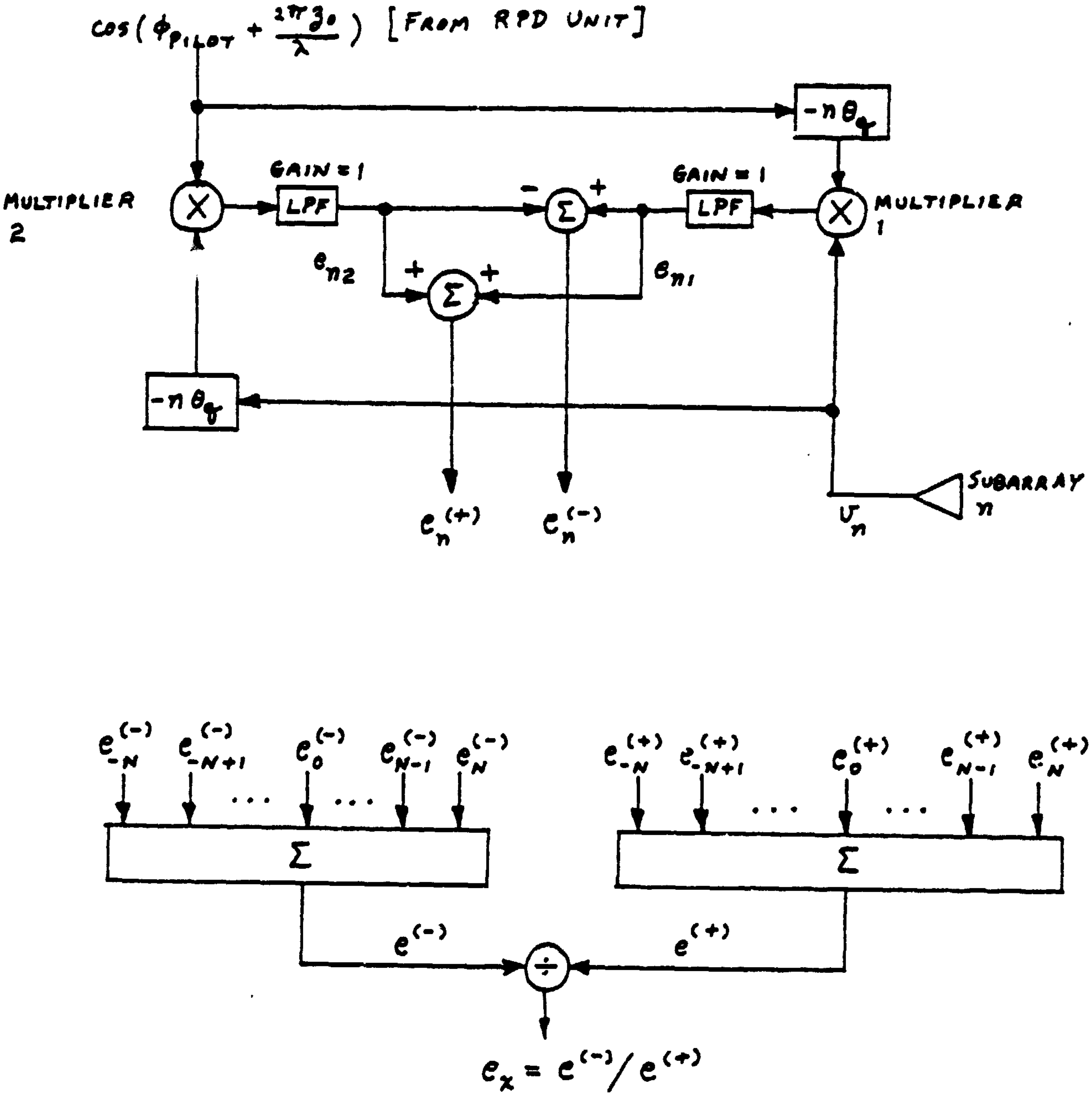

Figure 4. Signal processor at : (a) a typical subarray, and (b) the array processor.

The signals $e_n^{(-)}$ and $e_n^{(+)}$ are assumed conveyed to a central processor for the array, as shown in Figure 4(b).

2.4 Array Signal Processing - No Errors

Suppose no tilt or displacement errors are present. Then $\theta_{xn}=0$, $\theta_{yn}=0$, and $z_n=0$ for all n. Now (10) becomes

$$\left.\begin{matrix} e_n^{(+)} \\ \\ e_n^{(-)} \end{matrix}\right\} = \frac{A_0}{2} G(\theta_x, \theta_y) \{\cos[n(\frac{2\pi X}{\lambda} \theta_x+\theta_q)] \pm\cos[n(\frac{2\pi X}{\lambda} \theta_x-\theta_q)]\}. \tag{11}$$

The signals $e^{(+)}$ and $e^{(-)}$ in Figure 4(b) become

$$\left.\begin{matrix} e^{(+)} \\ \\ e^{(-)} \end{matrix}\right\} = \frac{A_0}{2} G(\theta_x, \theta_y) \{\frac{\sin[\frac{M}{2}(\frac{2\pi X}{\lambda} \theta_x+\theta_q)]}{\sin[\frac{1}{2}(\frac{2\pi X}{\lambda} \theta_x+\theta_q)]} \pm \frac{\sin[\frac{M}{2}(\frac{2\pi X}{\lambda} \theta_x-\theta_q)]}{\sin[\frac{1}{2}(\frac{2\pi X}{\lambda} \theta_x-\theta_q)]}\} \tag{12}$$

where

$$M=2N+1 \tag{13}$$

and we have used the known series

$$\sum_{n=-N}^{N} \cos(n\beta) = \frac{\sin[\frac{2N+1}{2} \beta]}{\sin(^{\beta}/_{2})} . \tag{14}$$

Next, define a subarray beamwidth (in rad) between -392dB points as θ_{sub}, given by

$$\theta_{sub} \overset{\Delta}{=} \lambda/X, \tag{15}$$

and

$$\bar{\theta}_q \overset{\Delta}{=} \theta_{sub}\, \theta_q/2\pi. \tag{16}$$

Then (12 becomes

$$\left.\begin{matrix} e^{(+)} \\ e^{(-)} \end{matrix}\right\} = \frac{A_0}{2} G(\theta_x, \theta_y) \{ \frac{\sin[\frac{M\pi}{\theta_{sub}}(\theta_x+\bar{\theta}_q)]}{\sin[\frac{\pi}{\theta_{sub}}(\theta_x+\bar{\theta}_q)]} \pm \frac{\sin[\frac{M\pi}{\theta_{sub}}(\theta_x-\bar{\theta}_q)]}{\sin[\frac{\pi}{\theta_{sub}}(\theta_x-\bar{\theta}_q)]} \}. \tag{17}$$

Now if we define an "array pattern" $G_a(\theta_x)$ by

$$G_a(\theta_x) = \frac{\sin[\frac{M\pi}{\theta_{sub}}\, \theta_x]}{M \sin(\frac{\pi\ \theta_x}{\theta_{sub}})} \approx \frac{\sin(\frac{M\ \pi\ \theta_x}{\theta_{sub}})}{(\frac{M\ \pi\ \theta_x}{\theta_{sub}})} \quad \text{for } |\theta_x| << \theta_{sub}/\pi \tag{18}$$

then

$$\left.\begin{matrix} e^{(+)} \\ e^{(-)} \end{matrix}\right\} = \frac{A_0 M}{2} G(\theta_x, \theta_y) \{G_a(\theta_x+\bar{\theta}_q) \pm G_a(\theta_x-\bar{\theta}_q)\}. \tag{19}$$

A sketch of $G_a(\theta_x)$ is shown in Figure 5 for $M=3,5$, and 9. The function is symmetric about $z=0$ and $\pm\ \pi$ and about $z=\pm\pi/2$. Thus, there is another peak in the function at $z=\pm\pi$. For M large $G_a(\theta_x)$ approaches a $\sin(x)/x$

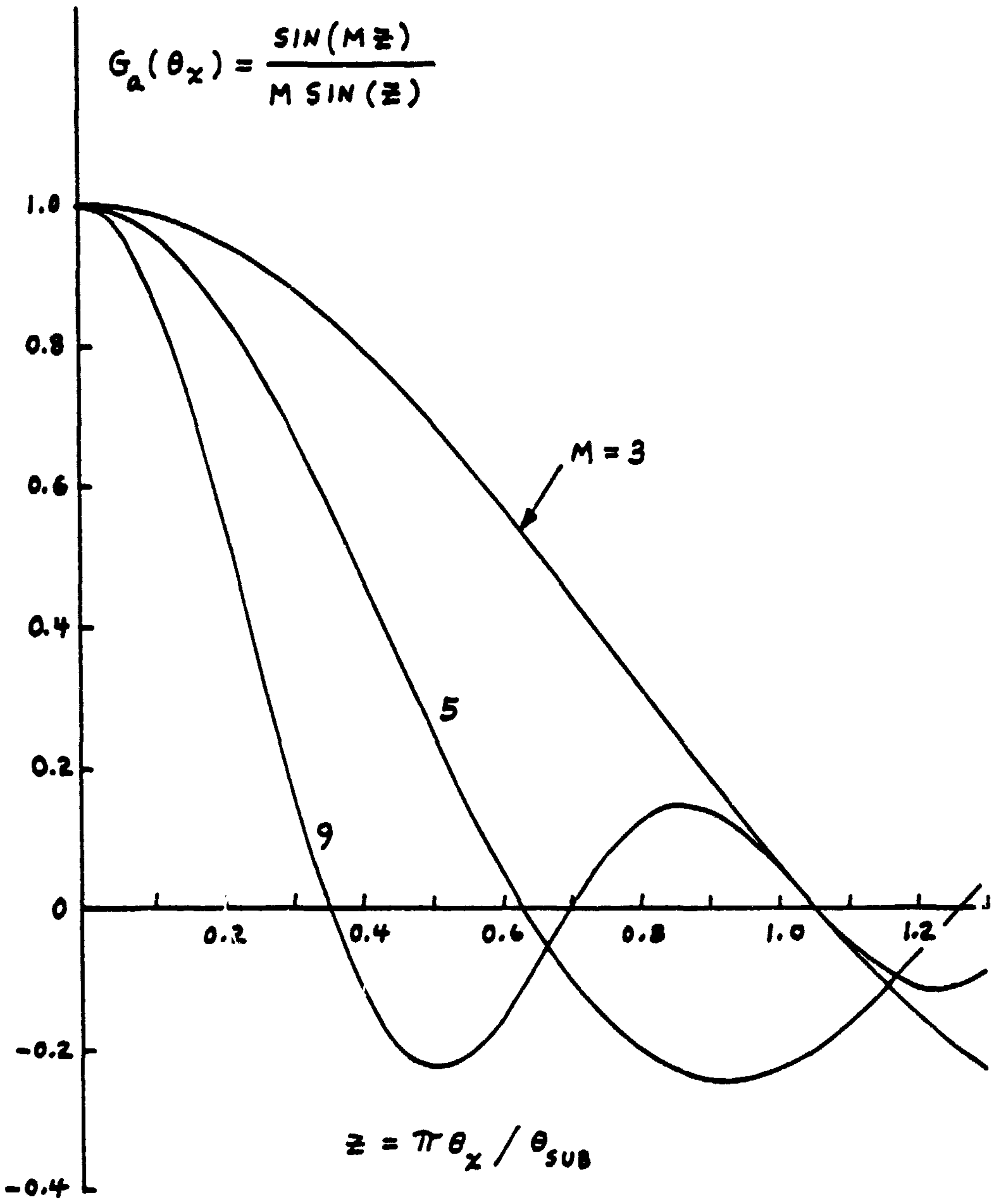

Figure 5. Array pattern.

function for small magnitudes of x. The responses (peaks) at $\pm\pi$ never show up in the response (17), however, because $G(\theta_x, \theta_y)=0$ for $z=\pi X\theta_x/\lambda = \pi\theta_x/\theta_{sub} = \pi$ from (7).

Next, define array sum and difference patterns by

$$G_\Sigma(\theta_x) \triangleq \frac{1}{2}\,[G_a(\theta_x+\bar{\theta}_q) + G_a(\theta_x-\bar{\theta}_q)] \tag{20}$$

$$G_\Delta(\theta_x) \triangleq \frac{1}{2}\,[G_a(\theta_x+\bar{\theta}_q) - G_a(\theta_x-\bar{\theta}_q)], \tag{21}$$

respectively. Equations of (19) become

$$\boxed{\begin{aligned} e^{(+)} &= A_0\, M\, G(\theta_x, \theta_y)\, G_\Sigma(\theta_x) && (22)\\ e^{(-)} &= A_0\, M\, G(\theta_x, \theta_y)\, G_\Delta(\theta_x). && (23)\end{aligned}}$$

The response e_x in Figure 4(b) becomes

$$\boxed{e_x = e^{(-)}/e^{(+)} = G_\Delta(\theta_x)/G_\Sigma(\theta_x).} \tag{24}$$

The behaviors of the sum, difference, and "normalized difference pattern" $G_\Delta(\theta_x)/G_\Sigma(\theta_x)$ are shown in Figures 6-9. In these figures we define an "array basic beamwidth" by

$$\theta_B \triangleq \theta_{sub}/M = \lambda/MX. \tag{25}$$

Figure 6 shows that the sum pattern can be of the usual single-peak form or double-peaked. The transition takes place when $\bar{\theta}_q/\theta_B = 0.6625$. Figure 7 shows typical difference channel responses with Figure 8 showing that the slope of the response at the origin is maximum when $\bar{\theta}_q/\theta_B$ is about 0.66. Figure 8 also shows the loss in gain of the sum channel as a function of

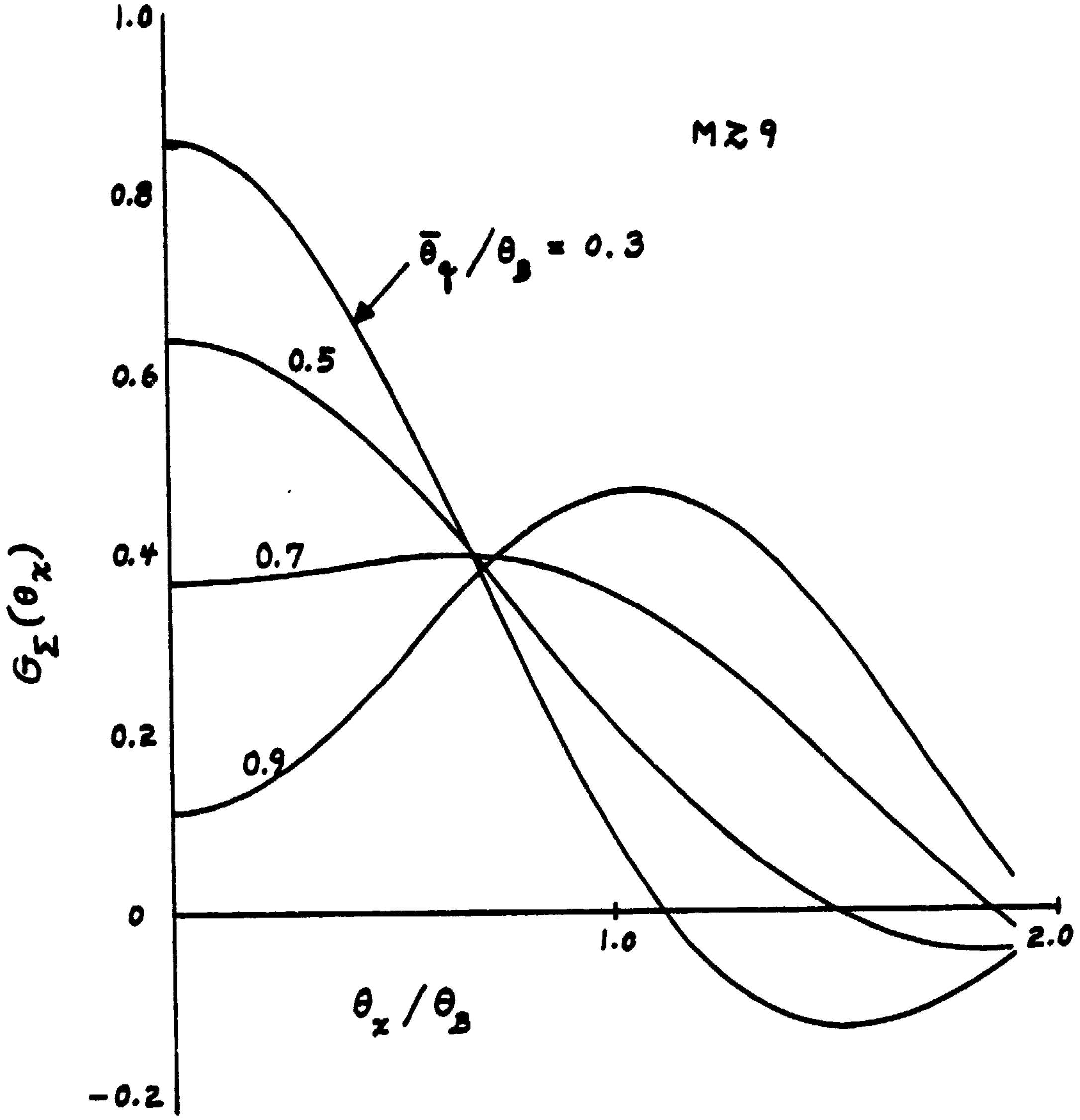

Figure 6. Sum pattern.

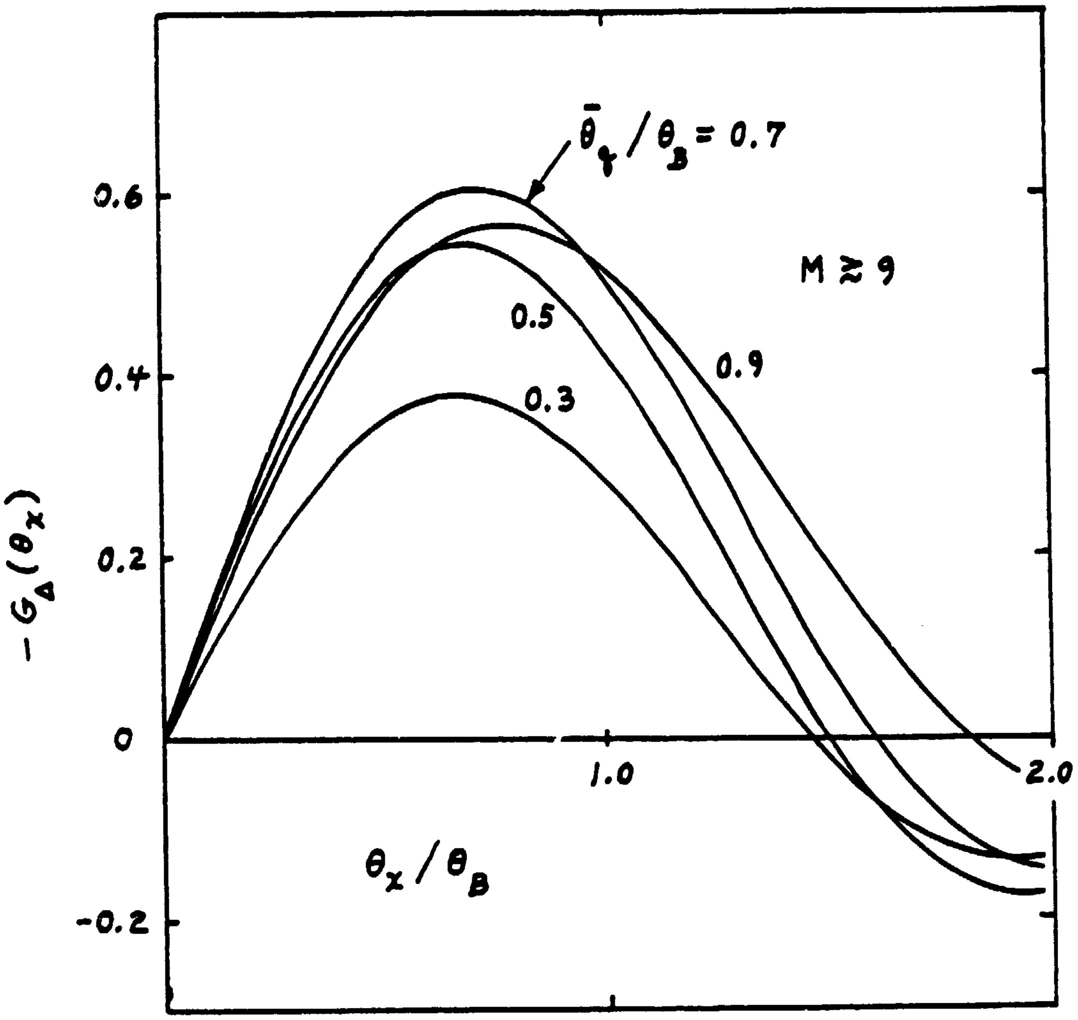

Figure 7. Difference pattern.

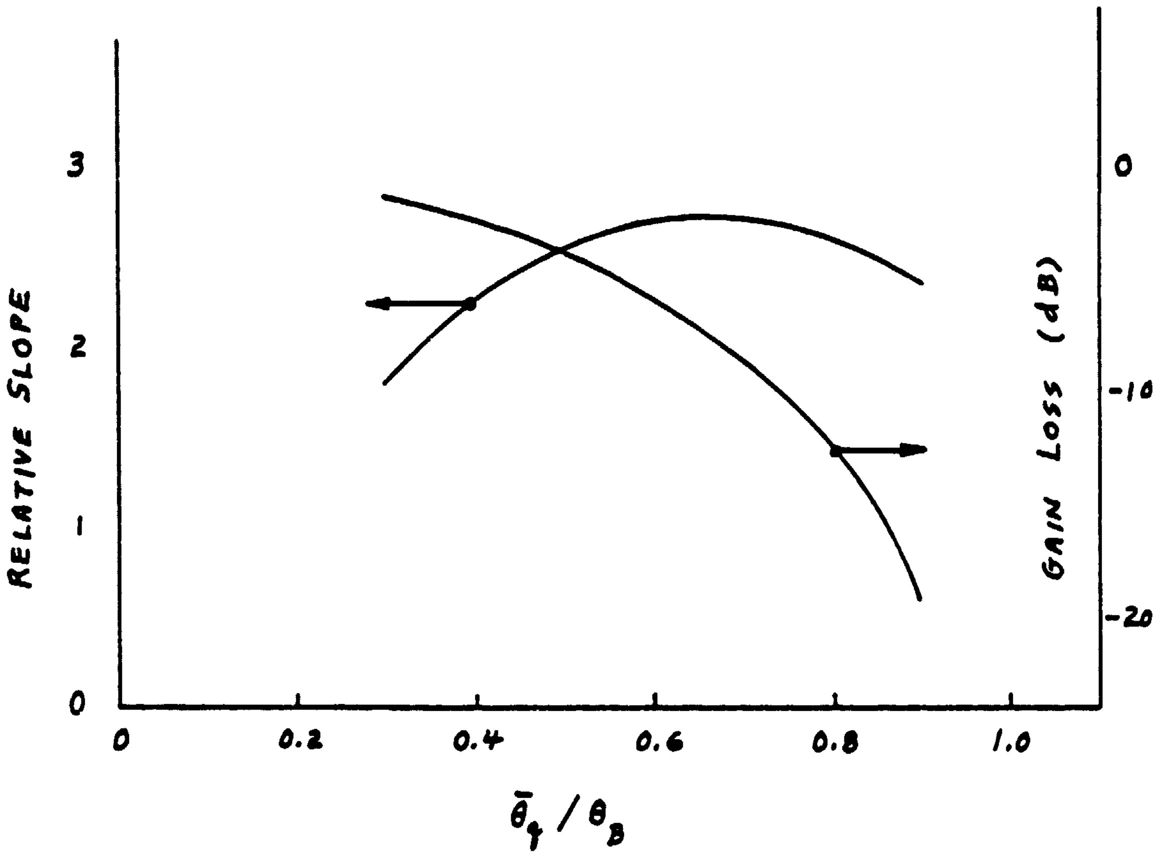

Figure 8. Slope of difference pattern and gain loss of sum pattern on boresight.

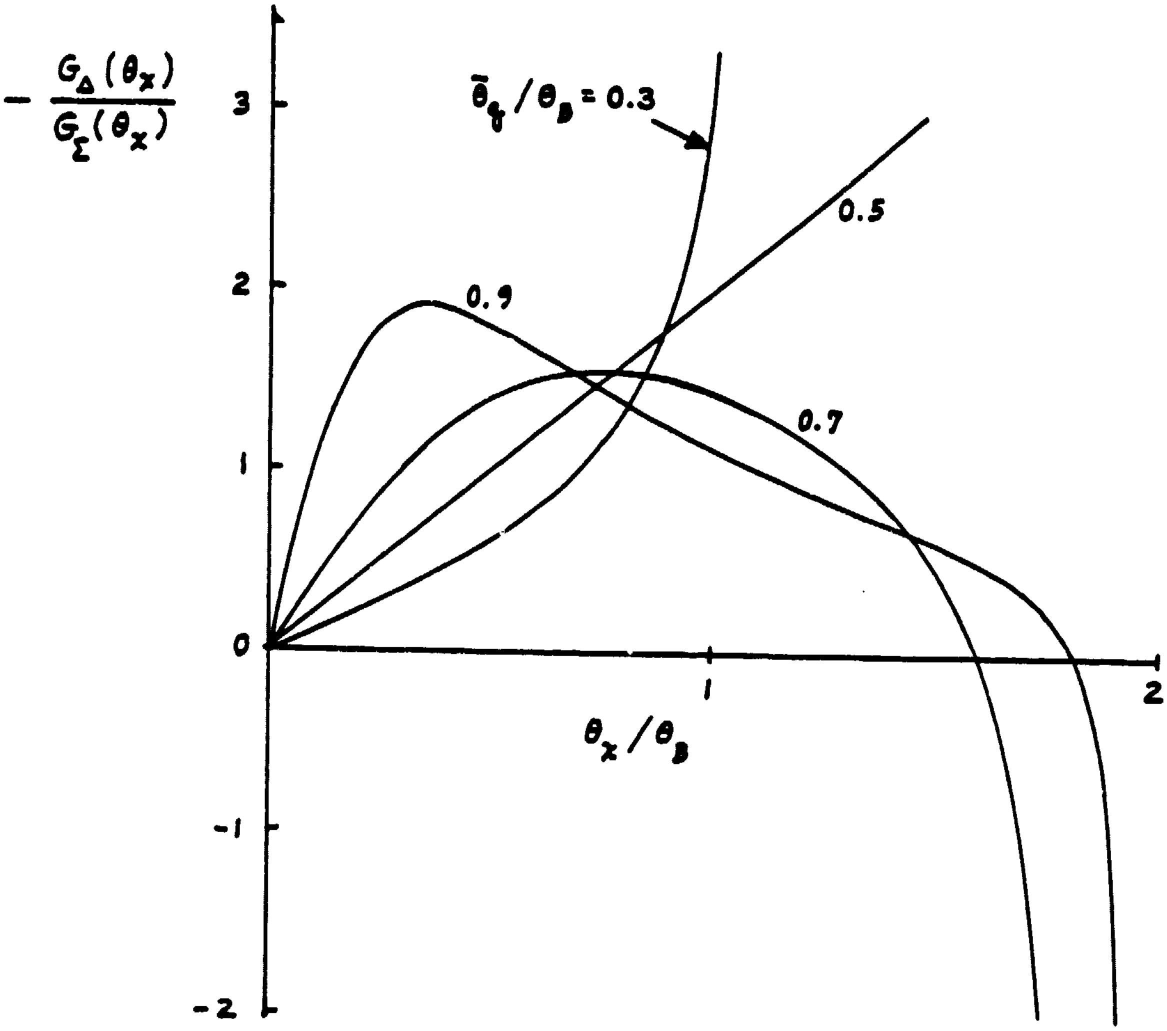

Figure 9. Normalized difference pattern.

$\bar{\theta}_q/\theta_B$. Finally, Figure 9 shows the normalized difference pattern. From these data, which apply for M larger than about 9, it is clear that $\bar{\theta}_q/\theta_B$ near 0.5 should be a good system choice based on small sum channel gain loss and beamwidth broadening, large error slope, and linearity of the normalized difference pattern.

For $\bar{\theta}_q/\theta_B = 0.5$ the slope of the difference pattern on boresight is

$$\text{slope} = \left.\frac{d\,G_\Delta(\theta_x)}{d\,\theta_x}\right|_{\theta_x=0} = \frac{-4}{\pi\,\theta_B} = \frac{-4\,M}{\pi\,\theta_{sub}} \,. \tag{26}$$

The slope of the normalized difference pattern on boresight is

$$\text{slope} = \left.\frac{d}{d\,\theta_x}\left[\frac{G_\Delta(\theta_x)}{G_\Sigma(\theta_x)}\right]\right|_{\theta_x=0} = \frac{-2}{\theta_B} = \frac{-2\,M}{\theta_{sub}} \,. \tag{27}$$

2.5 Effects of Noise

Assume each subarray output contains a bandpass gaussian noise $N_n(t)$. Such noises can be described by [2]

$$N_n(t) = N_{an}(t)\cos[\omega_{pilot}\,t] - N_{bn}(t)\sin[\omega_{pilot}\,t] \tag{28}$$

where $N_{an}(t)$ and $N_{bn}(t)$ are independent, gaussian random variables for any t and a given value of n. They are also independent between subarrays (different values of n). Furthermore $E[N_n^2(t)] = E[N_{an}^2(t)] = E[N_{bn}^2(t)] \triangleq \sigma_N^2$ is the noise power (assumed the same at each subarray).

Straightforward analysis of Figure 4(a), assuming the LPF's pass the full noise bandwidth, gives the noises present in $e_n^{(+)}$ and $e_n^{(-)}$, denoted $N_n^{(+)}$ and $N_n^{(-)}$, respectively.

$$N_n^{(+)}(t) = [N_{an}(t)\cos(\theta_T) + N_{bn}(t)\sin(\theta_T)]\cos(n\theta_q) \tag{29}$$

$$N_n^{(-)}(t) = [N_{an}(t)\sin(\theta_T) - N_{bn}(t)\cos(\theta_T)]\sin(n\theta_q) \qquad (30)$$

Here $\phi_{pilot}(t) = \omega_{pilot}\, t + \theta_T$, where θ_T is an arbitrary pilot source phase angle.

After summing the various noises as implied in Figure 4(b) the noises on the signals $e^{(-)}$ and $e^{(+)}$, denoted $N^{(-)}(t)$ and $N^{(+)}(t)$, respectively, are found. The powers in these noises follow taking the mean-squared values:

$$\sigma_\Sigma^2 \triangleq E[\{N^{(+)}(t)\}^2] = \sigma_N^2\left[\frac{M}{2} + \frac{1}{2}\frac{\sin(M\,\theta_q)}{\sin(\theta_q)}\right] \qquad (31)$$

$$\sigma_\Delta^2 \triangleq E[\{N^{(-)}(t)\}^2] = \sigma_N^2\left[\frac{M}{2} - \frac{1}{2}\frac{\sin(M\,\theta_q)}{\sin(\theta_q)}\right]. \qquad (32)$$

Figure 10 plots (31) and (32) versus $\overline{\theta}_q/\theta_B = M\,\theta_q/2\pi$. Clearly, for squint angles of interest ($\overline{\theta}_q = \theta_B/2$) we have $\sigma_\Sigma^2 = \sigma_\Delta^2$ so output noise powers are equal:

$$\sigma_\Sigma^2 = \sigma_\Delta^2 = M\,\sigma_N^2/2, \qquad \overline{\theta}_q/\theta_B = 0.5. \qquad (33)$$

2.6 Effect of Vibration (Displacement) Errors

We assume that there is symmetry in the vibration of the overall array so that the geometry of Figure 11 applies. Since subarray positions are

$$x_n = n\,X, \quad -N \le n \le N, \qquad (34)$$

then

$$z_n = z(x_n) = \Delta z\cos[(2K-1)\,\pi\,X\,n/D]. \qquad (35)$$

For small displacements $\Delta z << D$, as is the case in practice, it is readily shown that the vibration induced tilt is

$$\theta_{xn} = \frac{-\Delta z(2K-1)\pi}{D}\sin[(2K-1)\,\pi\,X\,n/D]. \qquad (36)$$

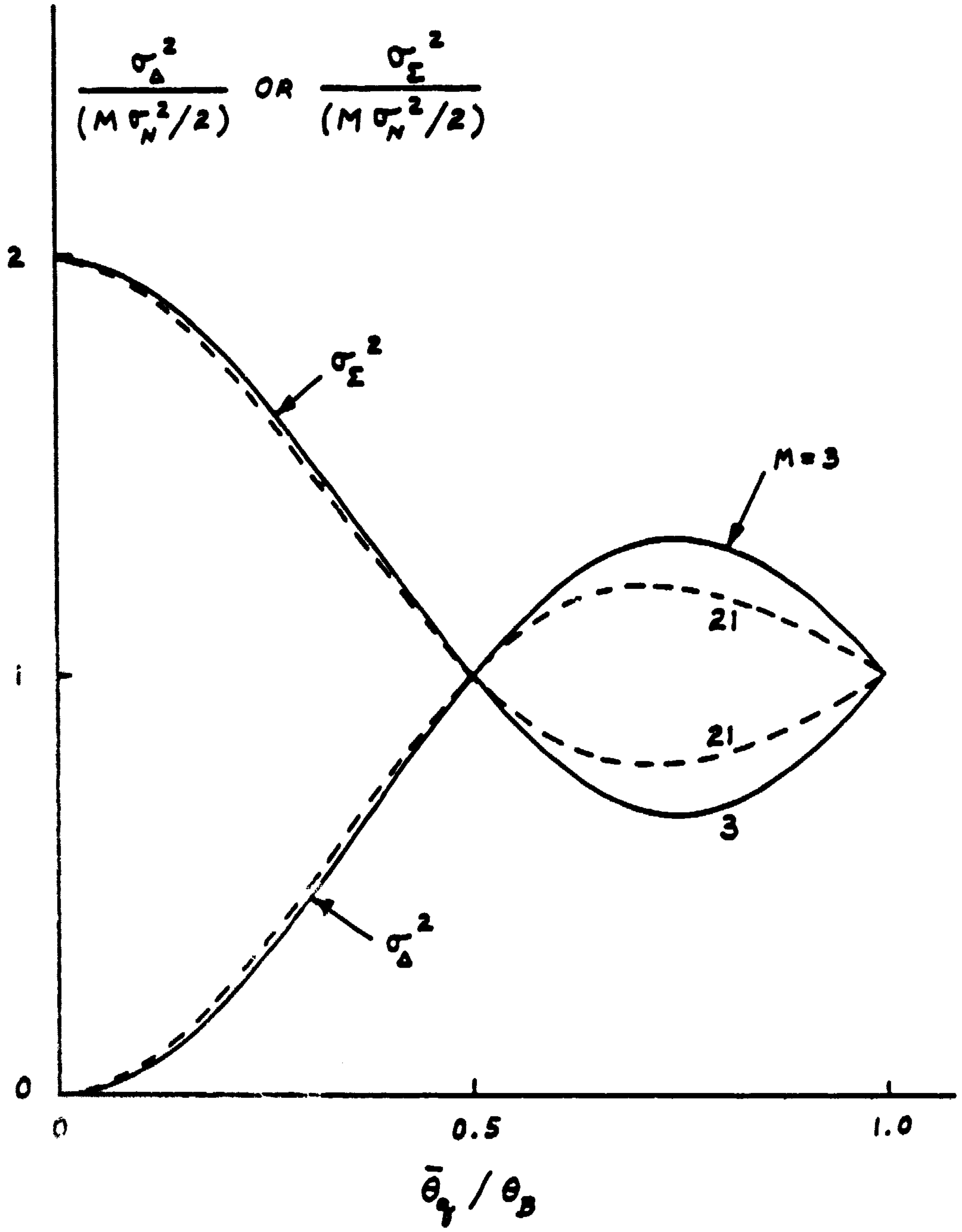

Figure 10. System noise powers.

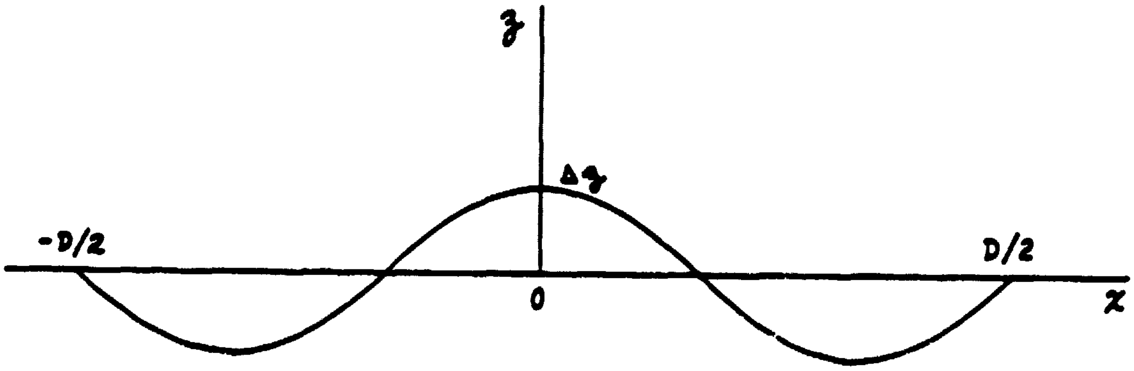

$$z(x) = \Delta z \cos[(2K-1)\pi x/D]$$

D = ANTENNA DIAMETER

K = VIBRATION MODE = 1, 2, ···

$$z_n = z(x_n) = \Delta z \cos[(2K-1)\pi X n/D]$$

$$\theta_{xn} = \frac{-\Delta z(2K-1)\pi}{D} \sin[(2K-1)\pi X n/D]$$

$$X_n = n X$$

Figure 11. Displacement on the antenna over a line through its center (origin).

Numerically, if $\Delta z = 1$ m, $D = 1010$ m, $X = 11.64$ m, and $\lambda = 0.1224$ m, then $|\theta_{xn}| \approx 0.89\ \theta_{sub}$, so tilt errors may be nearly as large as the subarray's beamwidth.

We evaluate vibration in the x direction when $\theta_y = 0$, $\theta_{yn} = 0$, and when

$$\Delta z = \overline{\Delta z}\cos(\omega_V t) \tag{37}$$

where $\omega_V/2\pi$ is the frequency of the vibrations. From (10), using (7), the signals $e^{(+)}$ and $e^{(-)}$ in Figure 4(b) are

$$\left.\begin{matrix} e^{(+)} \\ \\ e^{(-)} \end{matrix}\right\} = \frac{A_0}{2}\sum_{n=-N}^{N} Sa[\pi X(\theta_x+\theta_{xn})/\lambda] \cdot \{\cos[n(\frac{2\pi X\theta_x}{\lambda} + \theta_q) + \frac{2\pi(z_n-z_0)}{\lambda}]$$

$$\pm \cos[n(\frac{2\pi X\theta_x}{\lambda} - \theta_q) + \frac{2\pi(z_n-z_0)}{\lambda}]\}. \tag{38}$$

For relatively small values of θ_x the system's response will be $e_x = e^{(-)}/e^{(+)}$. However, the true response without vibration will very nearly equal the slope when $\theta_x = 0$ times θ_x, so that the "error" in radians produced by vibration, denoted θ_V, will be approximately

$$\theta_V = -[\frac{\theta_{sub}}{2\ M}\frac{e^{(-)}}{e^{(+)}} + \theta_x] = -[\frac{\lambda}{2MX}\ \frac{e^{(-)}}{e^{(+)}} + \theta_x], \tag{39}$$

after (27) is used. If normalized to the array basic beamwidth θ_B we have

$$\frac{\theta_V}{\theta_B} = -\frac{e^{(-)}}{2\ e^{(+)}} - \frac{\theta_x}{\theta_B} \tag{40}$$

while (38) becomes (for $\overline{\theta}_q = 0.5\ \theta_B$)

$$\left.\begin{matrix} e^{(+)} \\ e^{(-)} \end{matrix}\right\} = \frac{A_n}{2} \sum_{n=-N}^{N} \mathrm{Sa}\left[\frac{\pi}{M\,\theta_B}(\theta_x + \theta_{xn})\right]$$

$$\cdot\left\{\cos\left[n\left(\frac{2\pi\,\theta_x}{M\,\theta_B} + \frac{\pi}{M}\right) + \frac{2\pi(z_n - z_0)}{\lambda}\right]\right.$$

$$\left.\pm \cos\left[n\left(\frac{2\pi\,\theta_x}{M\,\theta_B} - \frac{\pi}{M}\right) + \frac{2\pi(z_n - z_0)}{\lambda}\right]\right\}. \qquad (41)$$

An examination of (41) shows that $e^{(-)} = 0$ if $\theta_x = 0$. Thus, for no antenna pointing error ($\theta_x = 0$) the presence of vibration produces no error, regardless of the vibration mode, so long as it is symmetric.

To study the error θ_V/θ_B when $\theta_x \neq 0$, (40) was computed on a digital computer for various values of M, K, and θ_x when peak vibration displacement in each case is 1.0 m. Figure 12 illustrates curves of θ_V as a percentage of array basic beamwidth θ_B versus the number M of subarrays in the array. Curves are shown for pointing error magnitudes $|\theta_x/\theta_B|$ of 0.05 and 0.1 for two vibration modes (K=1,2). The curves assume X=11.64 m, D=1012.68 m, and λ=0.1224 m. It is clear that some combinationsof vibration mode and pointing error give rise to large errors due to vibration.

For example, with M=7 subarrays in the linear array and mode 2 vibration (K=2), when pointing error θ_x is 5% of the array's basic beamwidth θ_B, the maximum error due to vibration of peak amplitude 1.0 m is 7.32% of θ_B. Figure 13 plots θ_B versus M and gives $\theta_B = 5.16\,\widehat{\min}$ for M=7. Thus, maximum error due to vibration is $0.0732\,(5.16) = 0.38\,\widehat{\min}$. Since the pointing error is $0.05\,(5.16) = 0.268\,\widehat{\min}$, we find the vibration error even exceeds the pointing error to be corrected by the servo system. The vibration error cycles with time, and, for the example taken here, is illustrated in Figure 14.

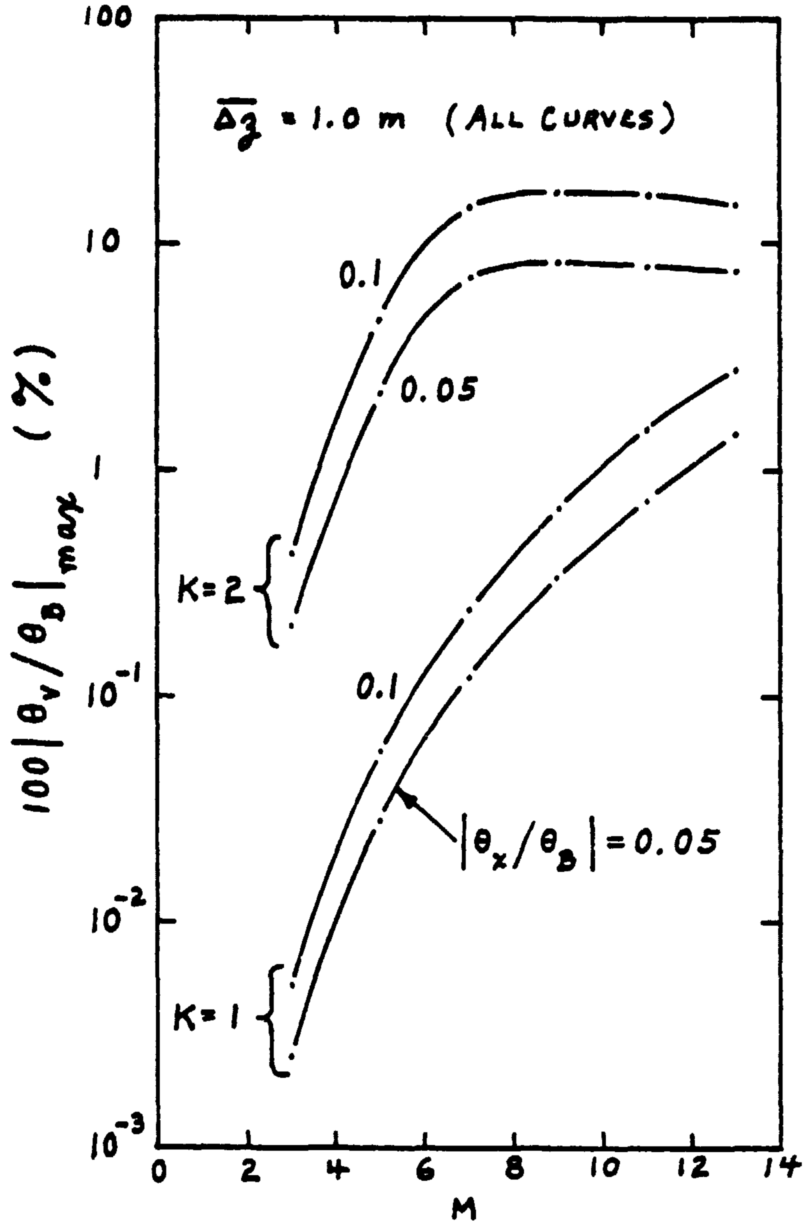

Figure 12. Error Θ_V due to vibration as a percentage on array basic beamwidth Θ_B.

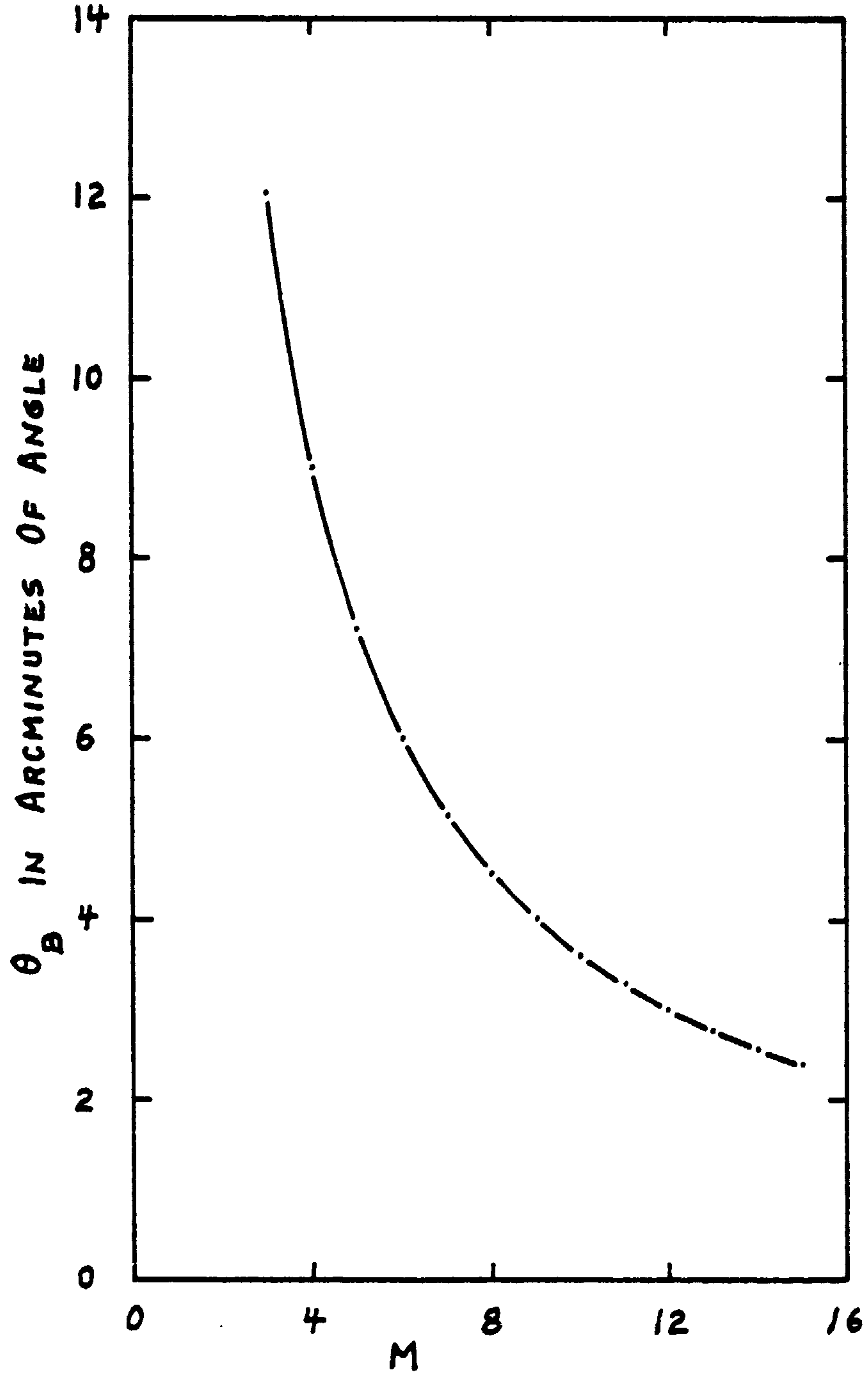

Figure 13. Array basic beamwidth Θ_B as a function of the number M of subarrays in a linear array.

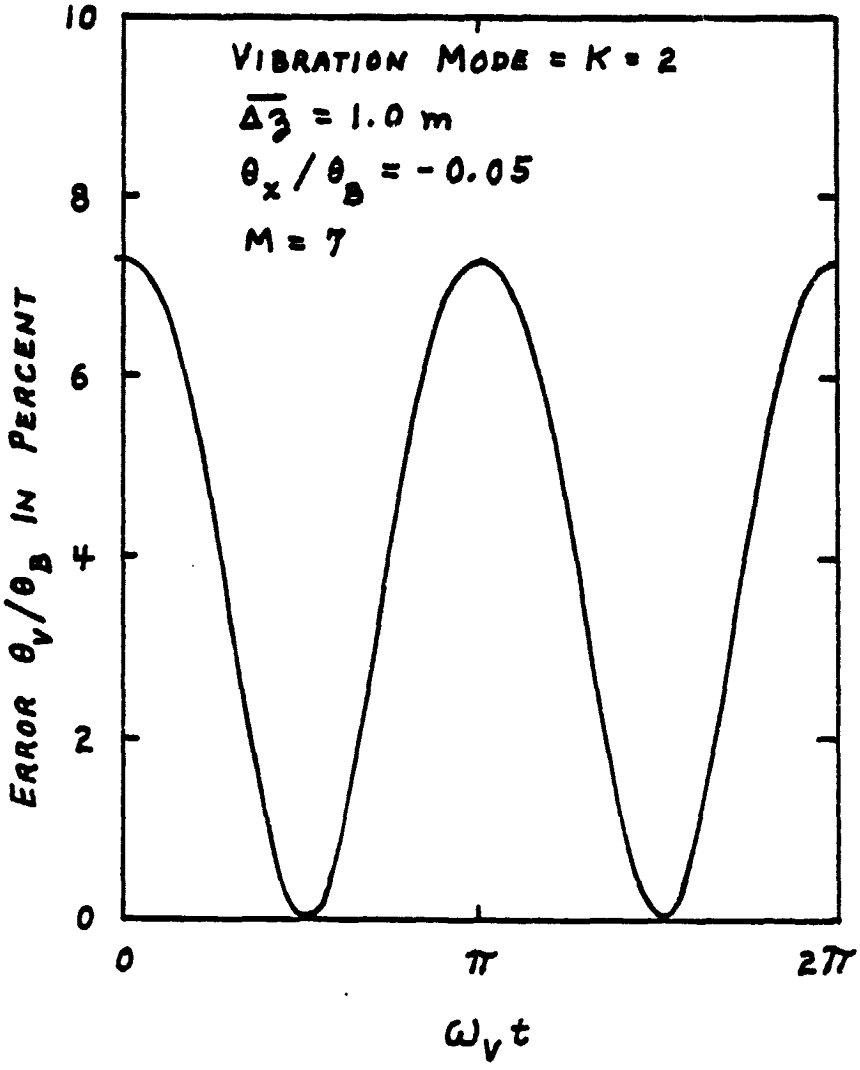

Figure 14. Error Θ_V due to vibration as a percentage of array basic beamwidth Θ_B.

Finally, we note that vibration will have an affect on signal-to-noise ratio of the composite signals $e^{(+)}$ and $e^{(-)}$. The affect on $e^{(+)}$ is of great concern since signal-to-noise ratio for this signal should be maintained above 10 to 100 for good performance of practical normalizing circuits. Figure 15 shows the maximum loss in this signal-to-noise ratio for various M, K, and θ_X/θ_B when $\overline{\Delta z} = 1.0$ m.

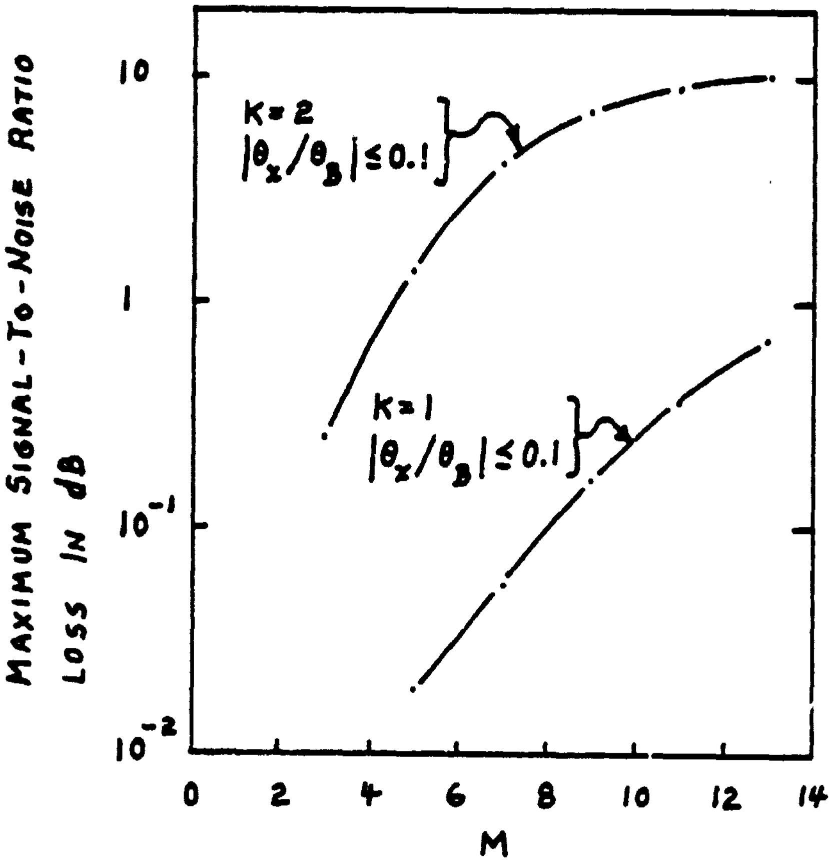

Figure 15. Signal-to-noise ratio loss due to vibration with $\overline{\Delta z}$ = 1.0m in all curves.

3. RIGID BODY ANTENNA POINTING CONTROL

In this section, an antenna pointing control system is modeled and then designed assuming that both the solar collector and antenna are rigid bodies. The purpose of this design is two-fold. First, the design will generate technical data such as motor requirements, system response time, effect of noise and system parameter changes, and the stiffness of the control loop. Second, by examining time constant of the control system and the mode frequencies of the flexible collector, the effect of the collector vibration mode on antenna pointing accuracy can be estimated. The goal of the mechanical pointing control is to maintain a mechanical pointing accuracy of three arc-minutes.

3.1 The Baseline Satellite Configuration

Figure 16 depicts the baseline satellite configuration. The dimension of the solar energy collector and the position of the microwave antenna are shown in Figure 16(a). The size and the general shape of the yoke-antenna combination is shown in Figure 16(b). Figure 16(c) is included to show the size of the rotary joint connecting the yoke to the solar collector.

The mechanical control of the antenna pointing is done by rotational motions about two axes. One rotational motion is about the Z_Y axis which is along the longitudinal center line of the collector as shown in Figure 16(a). A second rotational motion is about the X_A axis which is along the direction of hinges joining the antenna and the yoke as shown in Figure 16(b).

Two coordinate frames are used in the sequel, one is the antenna frame (X_A, Y_A, Z_A) and the other is the yoke frame (X_Y, Y_Y, Z_Y).

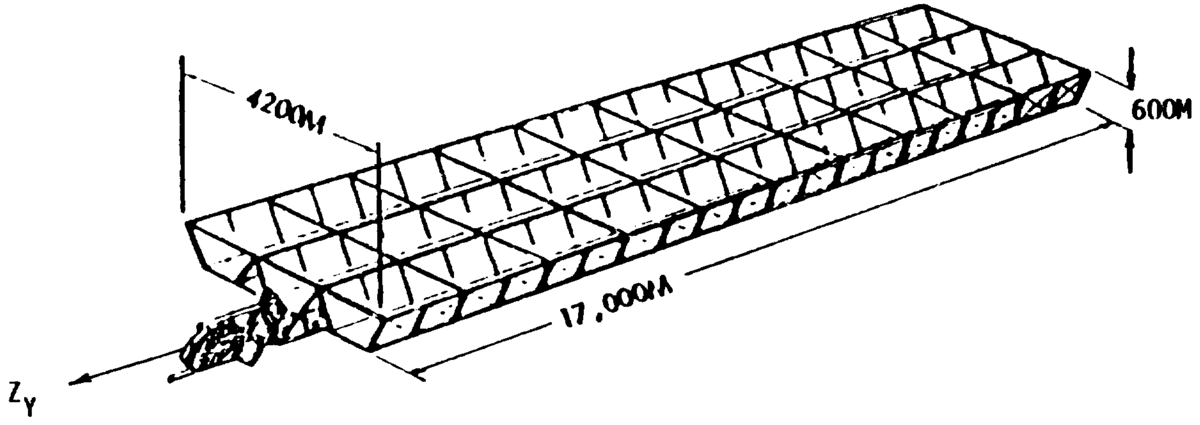

(a) SPS satellite

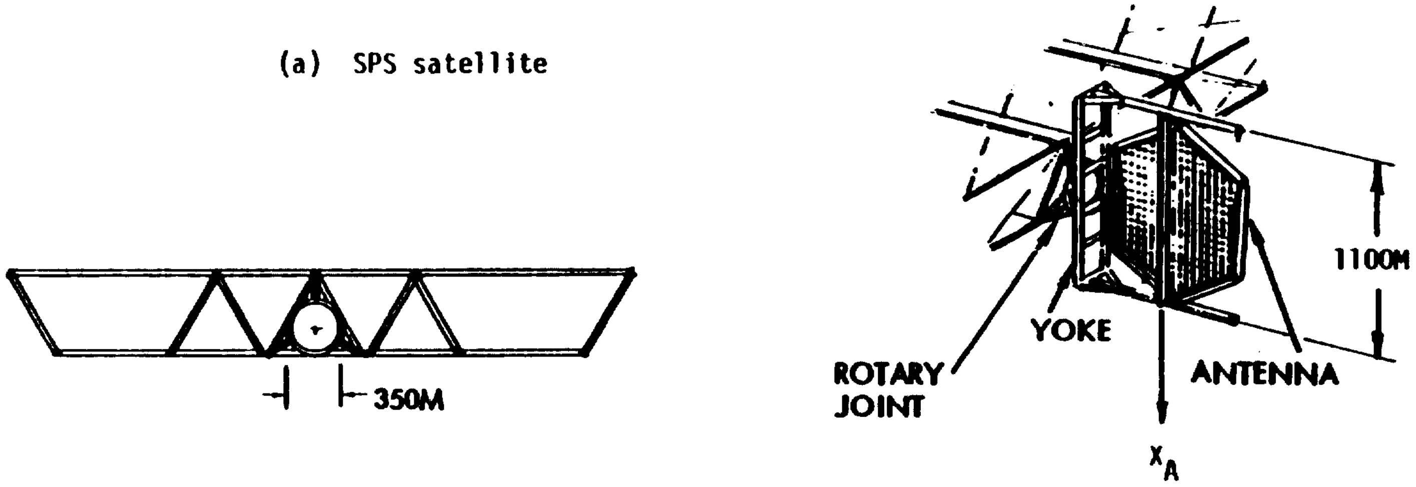

(c) The rotary joint

(b) Antenna and yoke

Figure 16. Baseline configuration for SPS satellite.

The physical parameters of the satellite are collected and listed here. For the collector:

Mass: $M_c = 16\text{x}10^6$ kg

Dimension $= \ell = 17{,}000$ m

$a = 4{,}200$ m

$b = 600$ m

moments of inertia =

$$(I_c)_{Z_Y} = \frac{M}{12}(a^2+b^2) = 19.5\text{x}10^{12} \text{ kg-m}^2$$

$$(I_c)_{X_A} = \frac{1}{3}M\ell^2 = 1.54\text{x}10^{15} \text{ kg-m}^2$$

For the combination of antenna and yoke:

Mass $= M_A = 13\text{x}10^6$ kg

Diameter: $D = 1{,}100$ m

Moments of inertia:

$$(I_A)_{Z_Y} = \frac{1}{4}MR^2 = \frac{1}{16}MD^2 = .983\text{x}10^{12} \text{ kg-m}^2$$

$$(I_A)_{X_A} = \frac{1}{4}MR^2 = .983\text{x}10^{12} \text{ kg-m}^2$$

Other physical data include:

slip-ring diameter = 350 m

motor shaft diameter = .1 m

gean-train ratio $\alpha = \frac{\text{Antenna speed}}{\text{motor speed}} = 10^{-4}$

The gear-train is used to connect the motor shaft to the rotary joint. Since the rotary joint has a diameter of 350 m and the motor diameter is .1 m, a gear-train ratio of 10^{-4} is reasonable.

3.2 Slip-ring Friction Characteristics

Conduction of electric power from the solar collector to the antenna yoke and from the yoke to the antenna is done by using slip-rings. The friction torque at each rotary joint is mostly due to the slip-ring friction torque which is a nonlinear function of speed of rotation. The nonlinear slip-ring friction characteristics, as provided by NASA/MSFC, are shown in Figure 17. In the figure θ represents the relative angular position between two sides of the rotary joint. The arrowheads indicate directions of motion. Notice that the friction torque has the saturation values of $\pm T_{max} = \pm 10^6$ N-M. In the region between the saturation values, the friction troque depends on θ in a way resembling the compliance torque. The compliance is the slope K_F which is -10^6 N-M per degree. The nonlinear friction torque exhibits the nature of shifting hysteresis.

Figure 18 gives two analog electronic circuits which can be used to simulate the above friction characteristics on an analog computer. For system simulation using a digital computer, however, neither one of these circuits are convenient to use. To provide a convenient way for later digital simulation, a digital simulation flow-diagram is developed as shown in Figure 19.

3.3 Estimation of Motor Parameters

It is assumed that d-c motors are used as torques for antenna pointing control. The rating for the d-c motors are estimated here. Assume a maximum perturbation angle for the antenna to be [3]

$$|\Delta\theta|_{max} = 1 \text{ degree} = .0175 \text{ radian}$$

The moment of inertia of the yoke-antenna load is

$$I_A = .983\times10^{12} \text{ kg-m}^2$$

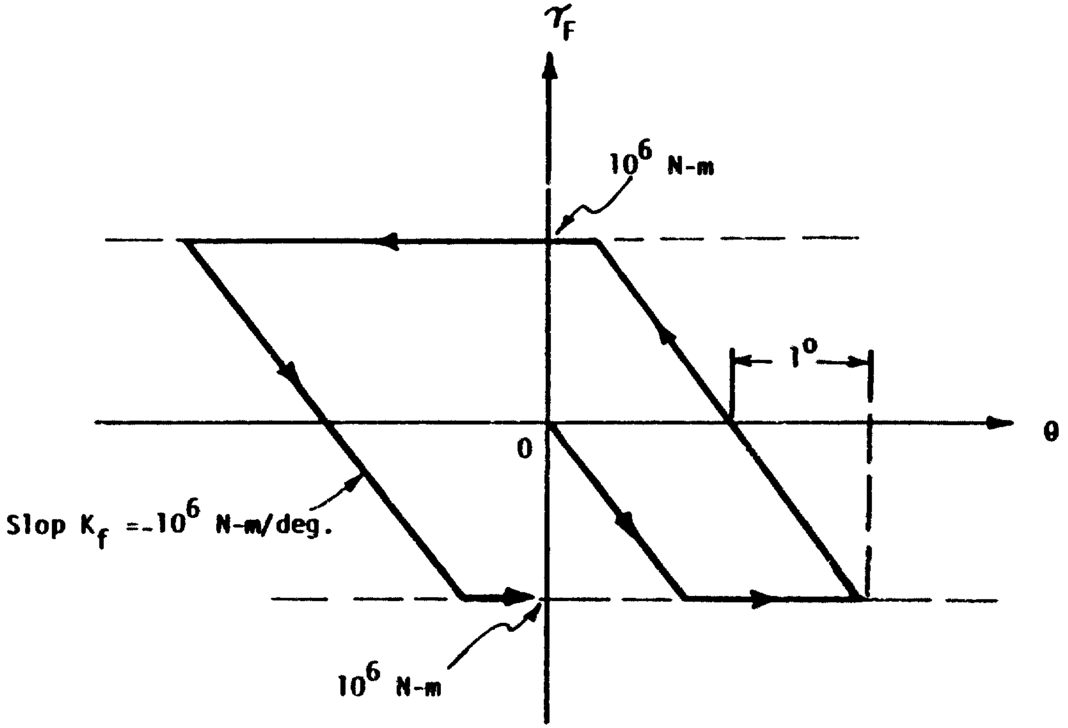

Figure 17. Slip-ring friction characteristics exhibits shifting hysteresis.

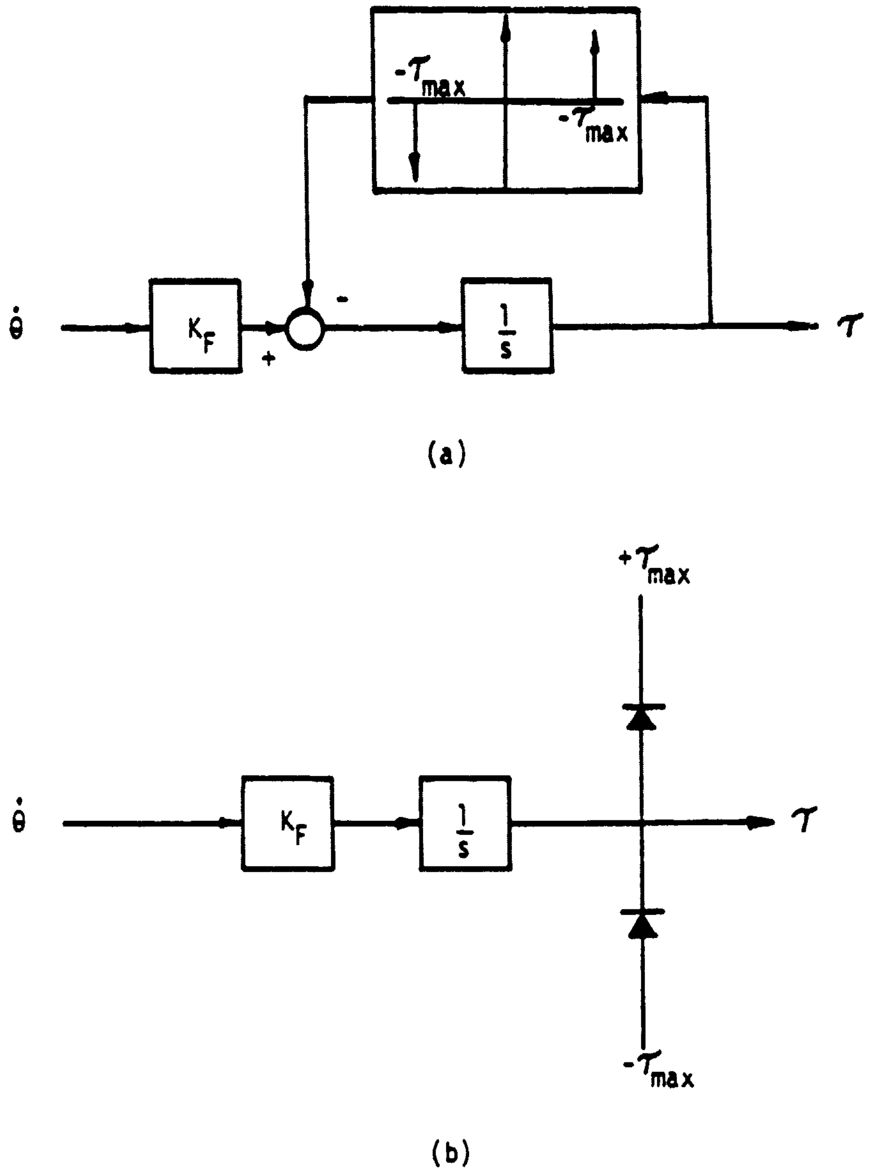

Figure 18. Analog circuits for the nonlinear slip-ring friction.

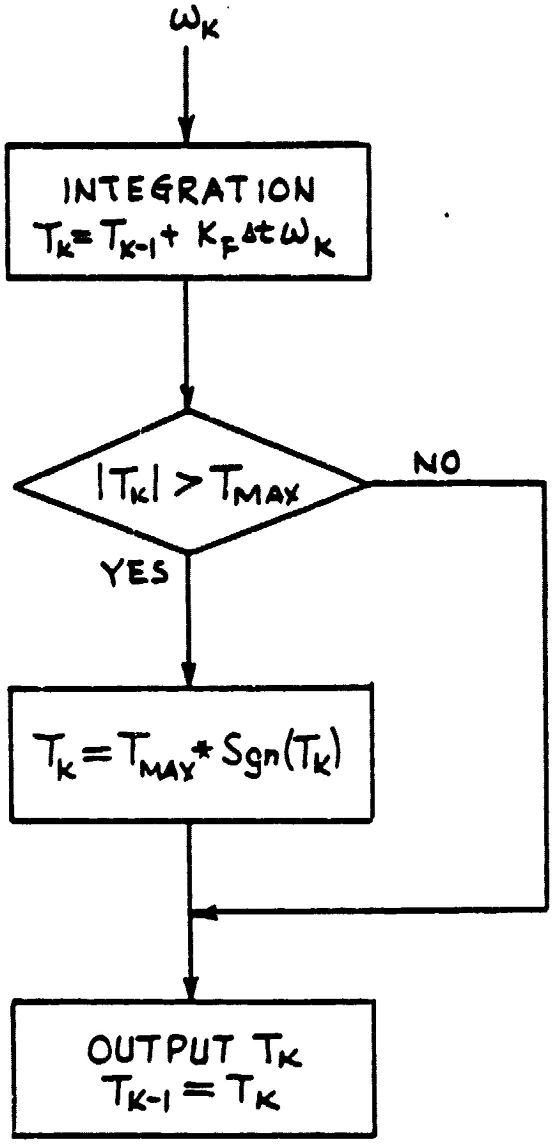

Figure 19. Digital simulation for slip-ring friction.

Given a gear-train ratio of $\alpha = 10^{-4}$, the reflected maximum angle perturbation and the moment of inertia of the load at the motor shaft is

$$I_A' = \alpha^2 I_A = 9830 \text{ kg-m}^2$$

$$|\Delta\theta'|_{max} = \frac{1}{\alpha}|\Delta\theta|_{max} = 175 \text{ radians}$$

(see discussion in Section 3.6).

The maximum slip-ring friction torque is

$$\begin{aligned} |\tau_F|_{max} &= 10^6 \text{ N-M at the ring} \\ &= \alpha \times 10^6 = 100 \text{ N-M at the motor shaft} \end{aligned}$$

The initial motor torque for a maximum step perturbation is

$$\begin{aligned} |\tau_0|_{max} &= I_A' \, |\ddot{\theta}|_{max} \\ &= \frac{I_A' \, |\Delta\theta'|_{max}}{T^2} = \frac{1.72 \times 10^6}{T^2} \text{ N-M} \end{aligned}$$

where T is the system time constant. Therefore the total maximum torque is

$$|\tau|_{max} = |\tau_F|_{max} + |\tau_0|_{max} = 100 + \frac{1.72 \times 10^6}{T^2} \qquad (42)$$

An estimate of motor power P is now given

$$\begin{aligned} P &= \text{Average of } [\Delta\dot{\theta}(t) \, \tau(t)] \\ &\leq |\dot{\theta}'|_{max} \, |\tau|_{max} \\ &= \frac{|\Delta\theta'|_{max} \, |\tau|_{max}}{T} \\ &= \frac{175}{T}\left(100 + \frac{17.2 \times 10^6}{T^2}\right) \\ &= \frac{1.75 \times 10^4 \, T^2 + 3 \times 10^8}{T^3} \text{ watts} \end{aligned} \qquad (43)$$

$$= \frac{23.46\ T^2+4.021\text{x}10^5}{T^3}\ \text{HP} \qquad (44)$$

Under the nominal condition the steady-state motor power is to overcome the slip-ring friction torque. This power is

$$P_0 = \frac{23.46}{T}\ \text{HP} \qquad (45)$$

A list of P and τ versus T is shown in Table 1. A baseline rating is chosen to be:

$P = 1681$ watts = 2.253 HP

$\tau = 578$ N-M

$T = 60$ seconds

Table 1. Motor Ratings

T (sec)	τ (N-M)	P(Watts)
10	17293	301750
30	2010	11694
60	578	1681
100	272	475
300	119	69
600	105	31
1200	101	15
1800	100	10

Adopting the baseline motor rating, motor parameters are now estimated. Take the effective d-c voltage to be

$$V_{dc} = 120\ \text{v.}$$

The average motor armature current is then

$$I_a = \frac{P}{V_{dc}} = \frac{1681}{120} = 14\ \mathrm{A}$$

The motor torque constant is

$$K_T = \frac{\tau}{I_a} = \frac{578}{14} = 41.3\ \frac{\mathrm{N\text{-}M}}{\mathrm{A}}$$

Using the MKS system of units, the motor emf constant equals the motor torque constant in value, giving

$$K_E = 41.3\ \mathrm{V\text{-}sec}$$

Assuming a 5% motor power loss, the motor armature resistance is computed by

$$R_a = \frac{.05P}{I_a^2} = .43\Omega$$

The result is summarized in Table 2 for the ease of future reference.

Table 2. Motor Parameters

Rated Power	1681 W
Rated Voltage	120 V
Torque constant, K_T	$41.3\ \frac{\mathrm{N\text{-}M}}{\mathrm{A}}$
Emf constant, K_E	41.3 V-sec
Armature resistance, R_a	.43 Ω

3.4 Effect of Centrifugal Force Induced Torque

Under the nominal condition the yoke-antenna assembly is rotating about the Z_Y axis of the SPS satellite at nearly constant speed. The rotation generates on each mass element of the antenna a centrifugal force which is directed perpendicularly to and away from the Z_Y axis. This force produces a torque about the X_A axis of the antenna, which may be viewed as a load disturbance torque for the pointing control system. This torque is analyzed with the help of Figure 20.

Let ΔM be the incremental strip of antenna mass as shown in Figure 20. Let Ω_E be the nominal angular velocity of the yoke-antenna assembly about the Z_Y axis, which is very close to the Earth's rate of rotation. The incremental torque about the X_A axis due to the centrifugal force on ΔM is

$$\begin{aligned}\Delta\tau_C &= (\Delta M)(\text{acceleration})(\text{torque arm})\\ &= (\sigma X_A\ \Delta Z_A)(\Omega_E^2\ Z_A \sin\theta)(Z_A \cos\theta) \qquad (46)\end{aligned}$$

where σ is the area mass density of the antenna, which is assumed constant. Integrating over the entire antenna plane gives centirfugal torque as

$$\begin{aligned}\tau_C &= \int_{\text{area}} d\tau_C = 4\int_0^R \sigma\ \Omega_E^2\ Z_A^2\ X_A \sin\theta \cos\theta\ dZ_A\\ &= 2\ \sigma\ \Omega_E^2 \sin 2\theta \int_0^R \sqrt{R^2 - Z_A^2}\ Z_A^2\ dZ_A\end{aligned}$$

where R is the radius of the antenna. After the integration the total centrifugal torque is obtained as

$$\tau_C = \frac{\pi}{8}\ \sigma\ \Omega_E^2\ R^4 \sin 2\theta \qquad (47)$$

Maximum torque occurs when $\theta = 45°$. The Earth's rotation rate is

$$\Omega_E = 15\ \text{deg/hour} = 7.27\times10^{-5}\ \text{rad/sec}$$

Using the baseline parameter values, $R = 550$ m and

$$\sigma = \frac{M_A}{\pi\ R^2} = \frac{13\times10^6}{\pi\times550^2} = 13.68\ \text{kg/m}^2$$

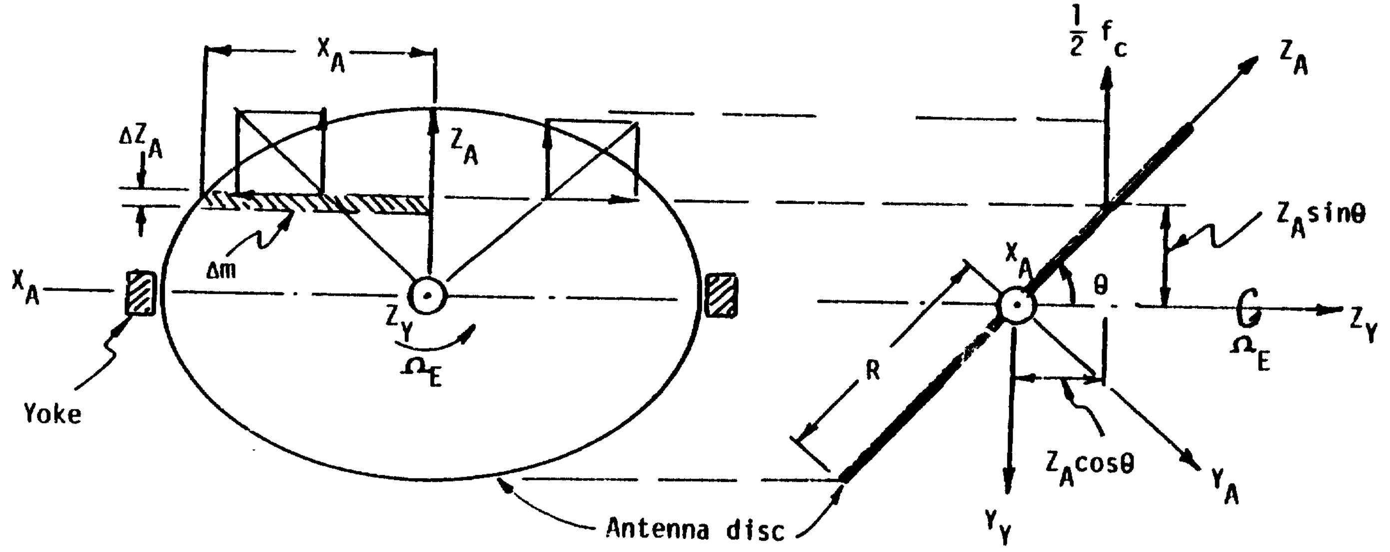

(a) Front view

(b) Side view

Figure 20. Centrifugal force induced torque.

Therefore the maximum torque is

$$|\tau_c|_{max} = 2598.2 \text{ N-m} \tag{48}$$

Comparing this torque to the maximum slip-ring friction torque, which is 10^6N-m, the former is less than .3% of the latter. The effect of the centrifugal force induced torque therefore needs no special attention, but may be lumped into the slip-ring friction torque as a perturbation. It is expected that such a small perturbation will not cause problems for the antenna pointing control. Computer simulation will be used to verify this fact.

3.5 Effect of Variation in Antenna's Moment of Inerita

Since the antenna disc may rotate about the X_A axis as indicated in Figure 21, its angular position θ about this axis may change. As a result, the antenna's moment of inertia about the Z_Y axis may change. It is desired that such change will not have adverse effects on the accuracy of the pointing control.

Let the moment of inertia matrix of the antenna expressed along the antenna frame (X_A, Y_A, Z_A) be

$$I = \begin{bmatrix} I_x & 0 & 0 \\ 0 & I_y & 0 \\ 0 & 0 & I_z \end{bmatrix}$$

Referring to Figure 21, the antenna frame and the yoke frame are related by an angle θ. The antenna's moment of inertia expressed along the yoke frame (X_Y, Y_Y, Z_Y) is

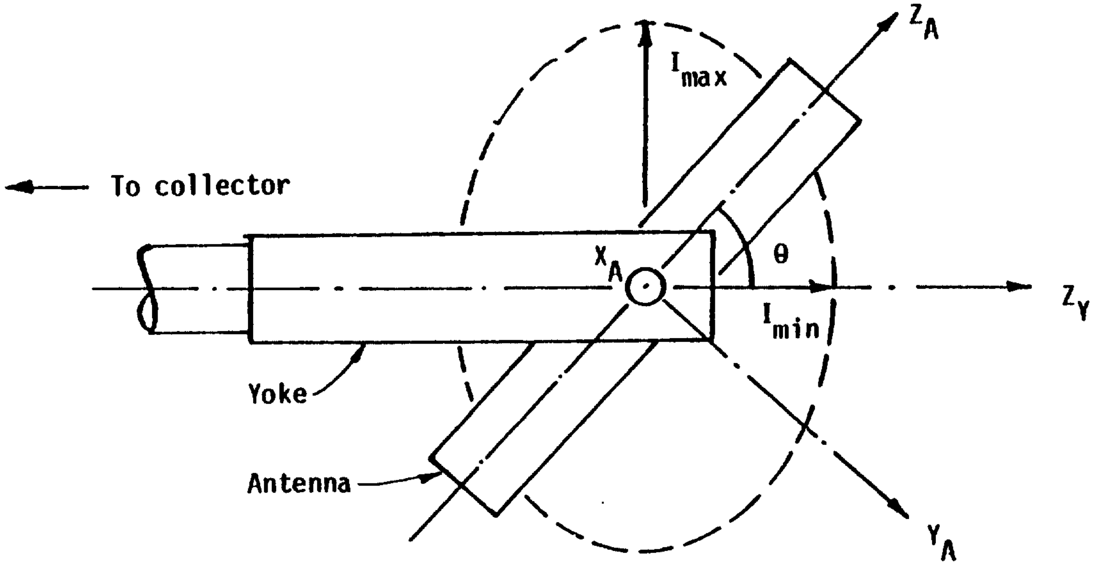

Figure 21. Variation in antenna's moment of inertia about Z_Y axis.

$$I' = \begin{bmatrix} 1 & 0 & 0 \\ 0 & c\theta & s\theta \\ 0 & -s\theta & c\theta \end{bmatrix} \begin{bmatrix} I_x & 0 & 0 \\ 0 & I_y & 0 \\ 0 & 0 & I_z \end{bmatrix} \begin{bmatrix} 1 & 0 & 0 \\ 0 & c\theta & -s\theta \\ 0 & s\theta & c\theta \end{bmatrix}$$

$$= \begin{bmatrix} I_x & 0 & 0 \\ 0 & I_y\, c\theta^2+I_Z\, s\theta^2 & -I_y \cos\theta+I_z s\theta c\theta \\ 0 & -I_y\, c\theta s\theta+I_z c\theta s\theta & I_y s\theta^2+I_z c\theta^2 \end{bmatrix} \tag{49}$$

where $c\theta = \cos\theta$ and $s\theta = \sin\theta$. In particular, the moment of inertia about the Z_Y axis is

$$I_z' = I_y\, s\theta^2+I_z\, c\theta^2 \tag{50}$$

Note

$$I_y = \frac{1}{2} M_A R^2 = \text{max, ant. mom. of inertia}$$

$$I_z = \frac{1}{4} M_A R^2 = \text{min. ant. mom. of inertia}$$

Taking the derivative of (50) with respect to θ

$$\frac{d}{d\theta} I_z' = 2\, s\theta\, c\theta\, I_y - 2\, s\theta\, c\theta\, I_z = (I_y - I_z)\sin 2\theta$$

Therefore the variation of the moment of inertia normalized with respect to I_z is

$$\frac{\Delta I'_z}{I_z} = \left(\frac{I_y}{I_z} - 1\right) \sin 2\theta\, \Delta\theta = \sin 2\theta\, \Delta\theta \tag{51}$$

For $\theta = 45°$, (51) is at its maximum. For $\Delta\theta = 1$ degree $= .0175$ radian, the specified attitude control accuracy for the SPS satellite,

$$\left[\frac{\Delta I_z'}{I_z}\right]_{max} = .0175 = 1.75\% \tag{52}$$

A plant parameter variation shown in (52) is too small to cause adverse effects in pointing control, and can be ignored in the design of pointing control. However, computer simulation will be performed to confirm this observation.

3.6 Pointing Control System Modeling

An all-attitude pointing control capability of the SPS antenna is made possible by allowing two degrees of rotational freedom for the antenna disc as shown in Figure 22. The first rotary joint allows the rotation of the antenna-yoke assembly with respect to the collector about the Z_Y axis, while the second rotary joint gives rotational freedom for the antenna with respect to the yoke about the X_A axis. It is assumed that the coupling of the antenna's motion about these two axis is negligible. This is due to the fact that the motion of the antenna is very slow and that the angular perturbations about the two axes are very small. Therefore the dynamics of the pointing control system for each rotary joint may be separately modeled.

The First Rotary Joint Let θ_A and θ_C be the absolute angular positions of the antenna-yoke assembly and the collector, respectively, about the Z_Y axis. Their dynamics are given by

$$I_A s^2 \theta_A = \tau' - \tau_F \tag{53}$$

$$I_C s^2 \theta_C = -\tau' + \tau_F \tag{54}$$

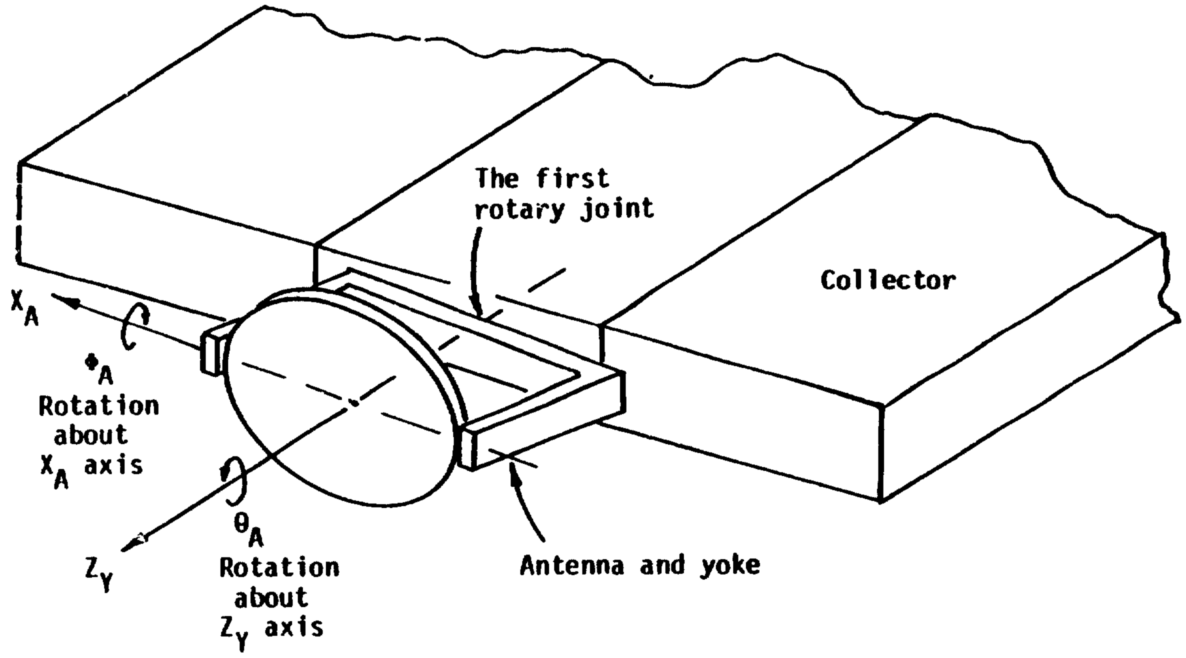

Figure 22. Two-axis antenna pointing control.

where I_A and I_c are moments of inertia of the antenna-yoke assembly and the collector, respectively; τ' is the control torque originated from the motor; and τ_F is the frictional torque of the slip-ring. Rotational compliance and other kinds of friction are assumed negligible. Adding (53) and (54) gives

$$I_A\theta_A+I_c\theta_c = 0 \tag{55}$$

Define the ratio of moments of inertia

$$\beta = \frac{I_A}{I_c} \tag{56}$$

Then (55) gives

$$\theta_c = -\beta\theta_A \tag{57}$$

The relationship among the generated torque τ, applied voltage V, and the shaft speed $s\theta$ for a separately excited d-c motor is

$$\tau = K_T\frac{V-K_E s\theta}{R_a} \tag{58}$$

where K_T, K_E and R_a are defined in Section 3.3. Noting the presence of a gear-train with a ratio α, the following relationships exist.

$$\theta = \frac{1}{\alpha}(\theta_A-\theta_c) = \frac{1}{\alpha}(1+\beta)\theta_A \tag{59}$$

$$\tau = \alpha\,\tau' \tag{60}$$

Ignore the nonlinear friction torque τ_F in (53) for the time being. Then

$$I_A\,s^2\,\theta_A = \tau' \tag{61}$$

Eliminating θ ,τ and τ' from (58), (59), (60) and (61), yield

$$\frac{K_T}{R_a}V = [(\alpha^2 I_A)s^2 + \frac{K_T K_E}{R_a}(1+\beta)s]\,\frac{\theta_A}{\alpha} \tag{62}$$

Let

$$I_A' = \alpha^2 I_A \tag{63}$$

which represents the reflected moment of inertia of the antenna-yoke assembly seen at the motor shaft. The transfer function of the first rotary system including the motor is therefore

$$\frac{\theta_A}{V} = \frac{\dfrac{\alpha\, K_T}{I_A' R_a}}{s\left[s+\dfrac{K_T K_E}{I_A' R_a}(1+\beta)\right]} \tag{64}$$

For later convenience, define

$$\theta_A' = \frac{\theta_A}{\alpha} \tag{65}$$

which is the reflected absolute attitute of the antenna-yoke as seen by the motor. Using (64) in (65) gives

$$G_p = \frac{\theta_A'}{V} = \frac{\dfrac{K_T}{I_A' R_a}}{s\left[s+\dfrac{K_T K_E}{I_A' R_a}(1+\beta)\right]} \tag{66}$$

Eq. (66) is the transfer function of the plant at the first rotary joint. Notice that the effect of the reaction motion of the finite mass collector is represented by β in the equation. For an infinite mass collector, $\beta=0$. A block diagram for this plant is given in Figure 23(a).

In sections 3.1 and 3.3, values of various parameters have been obtained as:

$I_A' = 9830$ kg-m^2 $\qquad R_a = .43\ \Omega$

$K_T = 41.3\ \frac{\text{N-m}}{\text{A}}$ $\qquad \alpha = 10^{-4}$

$K_E = 41.3$ V-s

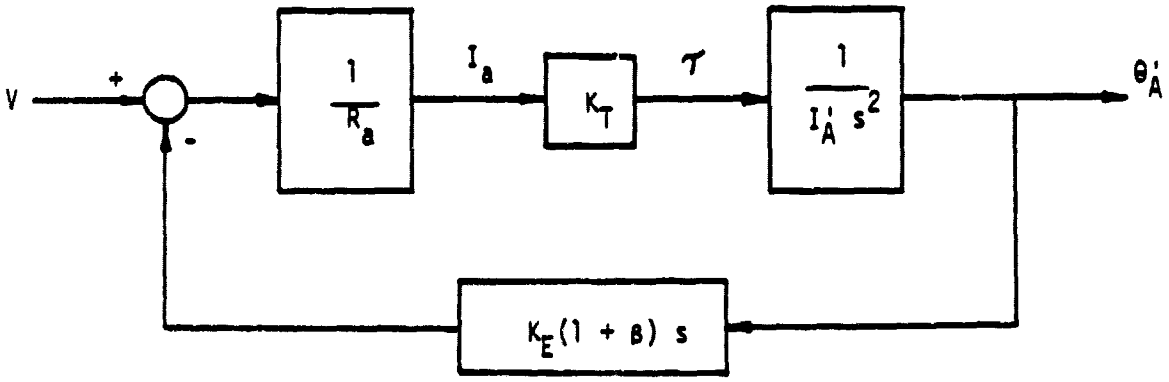

(a) First rotary joint

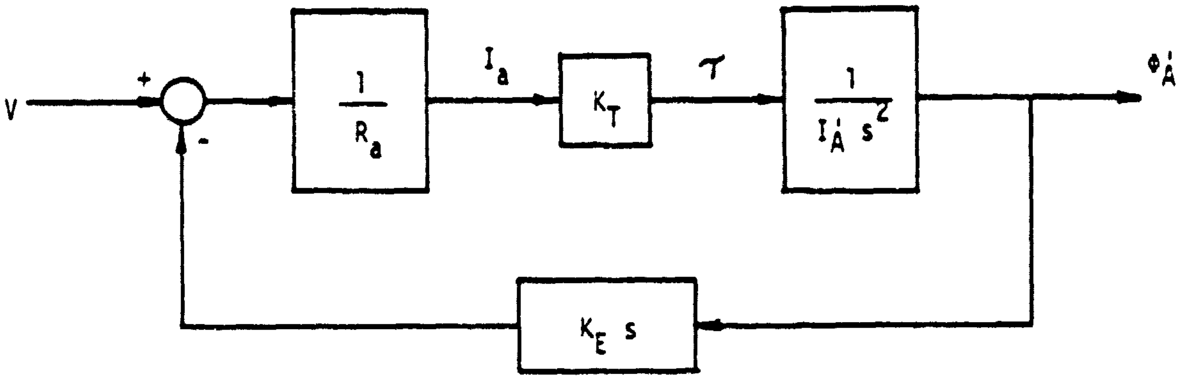

(b) Second rotary joint

Figure 23. Block diagram for controlled plants.

Quantity β as defined by (56) has a value of

$$\beta = \frac{.983 \times 10^{12}}{19.5 \times 10^{12}} \approx .05$$

With numerical values inserted, (66) becomes

$$G_p = \frac{\theta_A'}{V} = \frac{.01}{s(s+.424)} \qquad (67)$$

In this model the nonlinear friction was not included. The effect of the nonlinear friction will be treated as a torque disturbance in the control system design.

The Second Rotary Joint For the control about the X_A axis at the second rotary joint, the collector's moment of inertia may be assumed infinite. This is demonstrated as follows. Referring to Figure 24 and using the baseline data given in Section 3.1, moments of inertia about X_A axis are:

For the antenna:

$$(I_A)_{X_A} = \frac{1}{4} M_A R^2$$

For the collector

$$\begin{aligned}(I_c)_{X_A} = \frac{1}{3} M_c \ell^2 &= \frac{1}{3}(1.231 M_A)(31R)^2 \\ &= 394.3\ M_A R^2 \\ &= 1577\ (I_A)_{X_A}\end{aligned}$$

Thus, a rotation of antenna about X_A by 1° causes a rotation of collector about X_A less than 3 arc-seconds. For a 3 arc-minute mechanical pointing accuracy, the assumption of infinite moment of inertia contributes only .11 arc-second error.

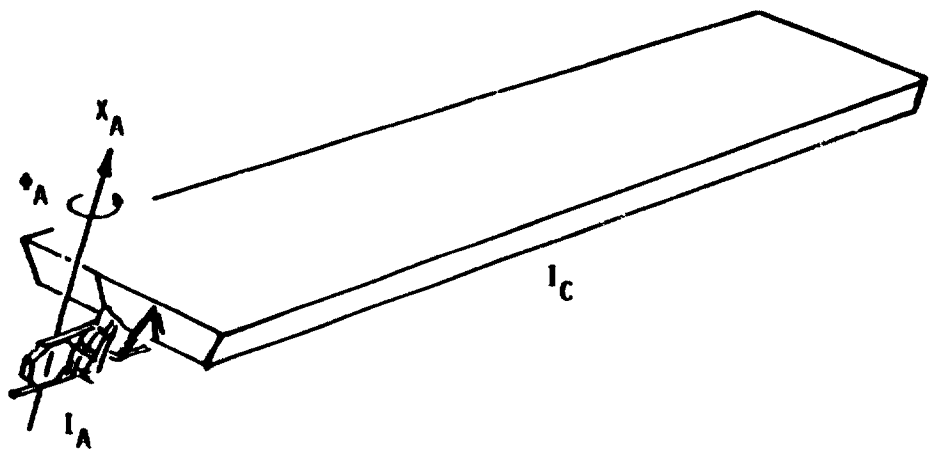

Figure 24. Moment of inertia about X_A axis.

The following are further assumed: (1) the same type of d-c motor will be used at the second rotary joint as the type used at the first rotary joint. (2) Same gear-ratio. (3) Mass of yoke is small as compared to that of antenna. Under this condition the transfer function for pointing control at the second rotary joint can be obtained from (66) by setting $\beta=0$, yeilding

$$G_p = \frac{\phi_A'}{V} = \frac{\frac{K_T}{I_A' R_a}}{s[s+\frac{K_T K_E}{I_A' R_a}]} \tag{68}$$

where θ_A' is the reflected antenna angle about the X_A axis as seen by the motor. The actual antenna angle is

$$\phi_A = \alpha \phi_A' \tag{69}$$

With numerical values inserted, (68) gives

$$G_p = \frac{\phi_A'}{V} = \frac{.01}{s(s+.404)} \tag{70}$$

A block diagram of the plant representing the second rotary axis is given in Figure 23(b).

3.7 Pointing Control System Design

Design Background

Under the assumption of negligible dynamical coupling between the two axes of rotation, the two associated control channels can be separately designed. The need of pointing control is to counter-act the effect of external disturbances and changes in plant parameters. External disturbances include gravity gradient torque, solar pressure torque, and collector motion coupled through the rotary joint. Change in plant parameters include the change in the antenna's moment of inertia due to change in antenna attitude, change in motor armature ressistance caused by thermal conditions, aging effects, change of structural shapes and dimensions due to temperature changes, and others. Most of the disturbances are constant or very low frequency cyclic. Parameter changes are also very low frequency in nature. It is assumed that the frequency range for disturbances and parameter changes is below .001 hertz (15 minutes per cycle). Effects of instrument noise will be ignored because they will be well attenuated by the low-pass characteristics of the system.

Under the nominal condition, the antenna-yoke is rotating at the first rotary joint with a constant rate of one revolution per 24 hours. Magnitudes of disturbances at this joint are assumed small so the direction of rotation is not reversed. The second rotary joint is stationary under the nominal condition. With disturbances added, it may rotate in either direction.

Comparing (67) and (70) shows that they differ only in time constant of an amount of less than 5%. Many well designed control loop for one plant should therefore perform well for the other. In view of this, a control system design will be made for (67), the plant for the first rotary joint.

Figure 25 depicts an antenna pointing control loop for the first rotary joint. An ideal gear-train is assumed. The pointing error is sensed by the microwave error sensing method presented in Section 2.1. An algorithm is used to generate, from the error signal, a command signal for pointing control. Three ways of generating command signal have been developed previously. [1] For the convenience of design the transfer function between error e and command signal may be taken to be unity. The present control system design is to determine the block labeled "network and amplifier gain".

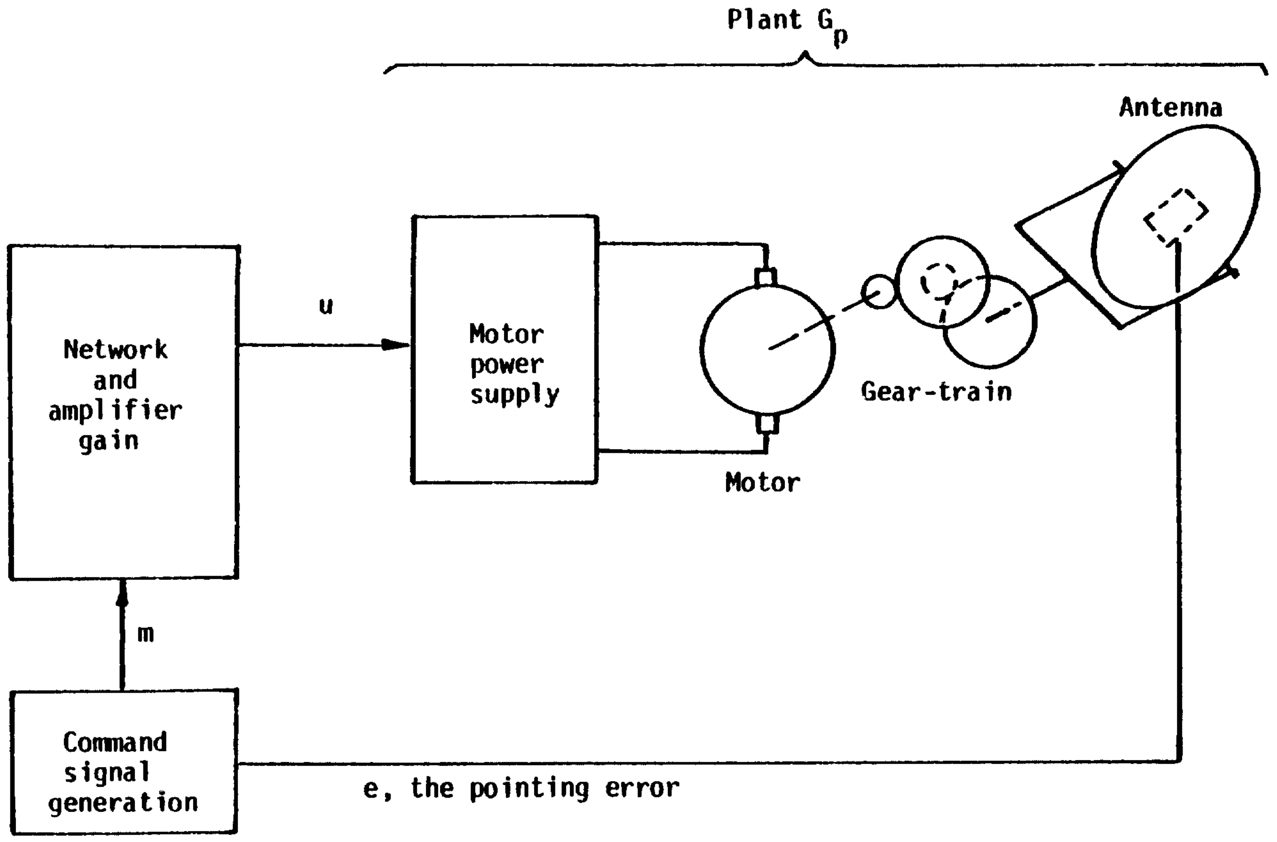

Figure 25. Antenna pointing control for the first rotary axis.

The Design Except for the 3 arc-minute mechanical pointing accuracy requirement, no other system performance specifications were given. Linear quadratic optimal control design will be adopted. Since the plant, represented by (67), has single-input and single output, frequency domain optimization by way of the root-square-locus technique will be used. [4] Because of the constant rate rotation under the nominal conditions, the control system for the first rotary joint should be a follow-up system. Follow-up design will also be used for the second rotary joint to provide flexibility for the possible need of follow-up operations.

Begin with (67), the plant transfer function*

$$G_p = \frac{.01}{s(s+.424)} \quad \left(\frac{1}{s}\right)$$

which has poles at $p_1=0$, $p_2=0$, and $p_3=-.424$. Open-loop poles for the root-square locus plot are

$$P_1 = - p_1 = 0$$
$$P_2 = - p_2 = 0$$
$$P_3 = - p_3 = - .18$$

There are no open-loop finite zeros. The root-square loci are shown in Figure 26. Choose the closed-loop root-square poles at

$$Q_1 \ \& \ Q_2 = .8 \pm j\,1.48$$
$$Q_3 = -.18 - Q_1 - Q_2 = -1.78$$

Then

$$-Q_1 \ \& \ -Q_2 = -.8 \pm j\,1.48$$
$$-Q_3 = 1.78$$

---

*An integrator is added to make the system type-2.

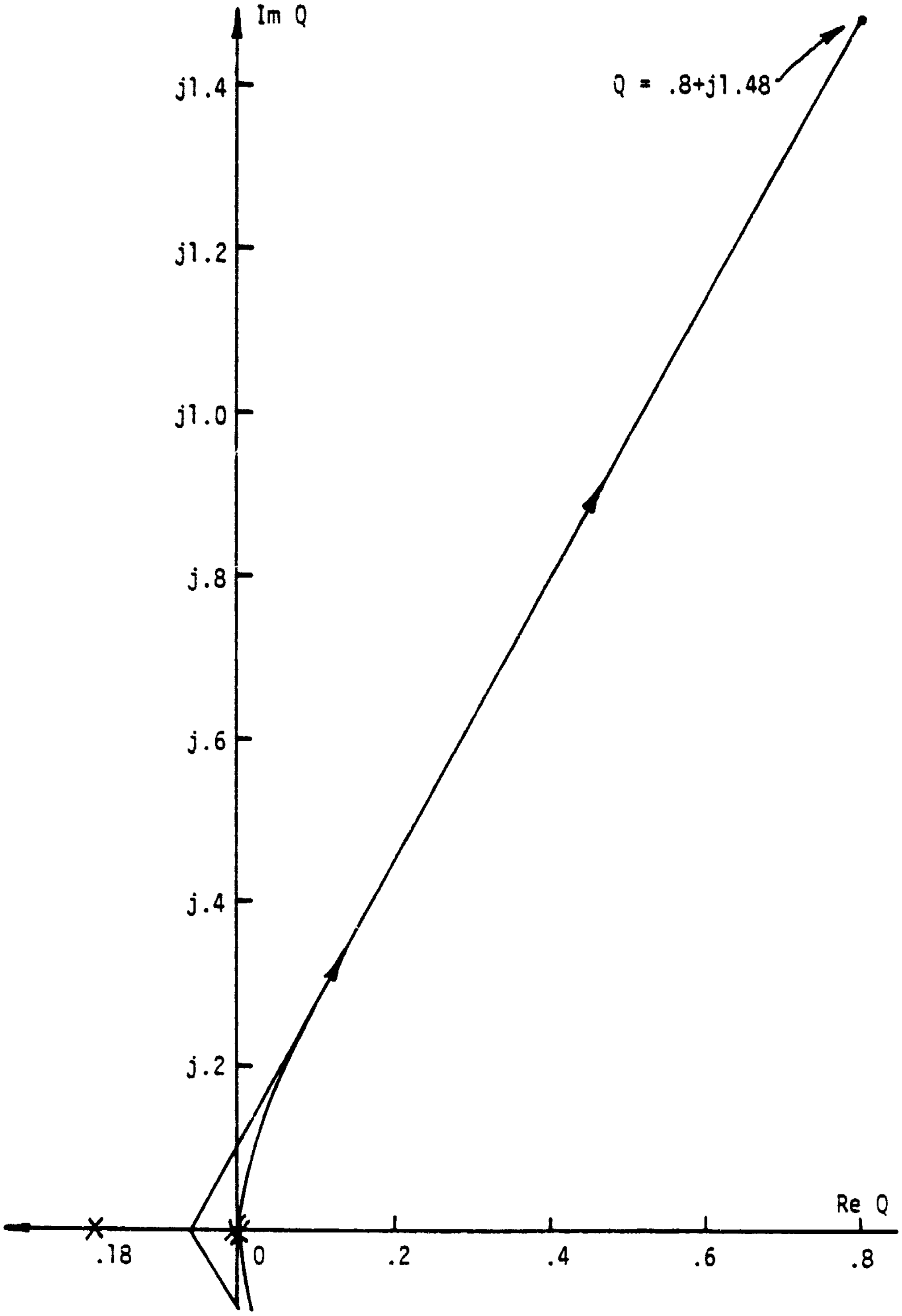

Figure 26. The root-square locus plot.

The closed loop poles for the control system are given by

$$\begin{aligned} q_1 &= -\sqrt{-Q_1} = 1.297\ |\underline{120.8} \\ q_2 &= -\sqrt{-Q_2} = 1.297\ |\underline{-120.8} \\ q_3 &= -\sqrt{-Q_3} = -1.33 \end{aligned} \tag{71}$$

Compute

$$q_1 q_2 = 1.682$$

$$q_1 + q_2 = -1.328$$

$$\frac{q_1 + q_2}{q_1 q_2} = -.79$$

The reciprocal of the closed loop zero is

$$T = -\left(\frac{1}{q_1} + \frac{1}{q_2} + \frac{1}{q_3}\right) = -\left(\frac{q_1 + q_2}{q_1 q_2} + \frac{1}{q_3}\right)$$

$$= .79 + .75 = 1.54$$

The closed-loop transfer function is

$$H = \frac{\theta'_A}{R} = \frac{(1+Ts)}{(1-\frac{s}{q_1})(1-\frac{s}{q_2})(1-\frac{s}{q_3})}$$

$$= \frac{1+Ts}{(1-\frac{s}{q_1})(1-\frac{q_1+q_2}{q_1 q_2}s + \frac{1}{q_1 q_2}s^2)}$$

$$= \frac{1 + 1.54\,s}{(1+.75s)(1+.79s + .595s^2)}$$

$$= \frac{1 + 1.54s}{1 + 1.54s + 1.18s^2 + .45\,s^3} \tag{72}$$

Step response simulation was performed to test (72). The overshoot was found to be more than 40%: not a good response. Repeated trial-and-error adjustment led to the following closed-loop transfer function.

$$H = \frac{e'_A}{R} = \frac{1 + 3.164s}{1 + 3.164s + 3.082s^2 + .595s^3} \qquad (73)$$

This system had a step responce overshoot of 18.7% and a time-to-peak of 3.4 seconds. The corresponding open-loop transfer function G_0 was obtained from

$$\frac{1}{H} = 1 + \frac{1}{G_0} \qquad (74)$$

giving

$$G_0 = \frac{.3245(1 + 3.164s)}{s^2(1 + .193s)} \qquad (75)$$

Two compensation configurations were used as shown in Figure 27; the first is a series compensation and the second is a series compensation with rate feedback. The second configuration offers better counter-action for load disturbance and plant parameter variation.

For series compensation:

$$G_c = \frac{G_0}{G_p} = 13.75 \; \frac{(1 + 3.164s)(1 + 2.36s)}{s(1 + .193s)} \qquad (76)$$

For series compensation with rate feedback:

$$\text{choose } K_T = 475.76 \doteq 476 \qquad (77)$$

$$\text{then } G_c = \frac{168.1(1 + 3.164s)}{s} \qquad (78)$$

A block diagram for the simulation of the designed closed-loop system is given in Figure 28. The dashed line part is used only for series compensation with rate feedback. Figure 29 shows the step response

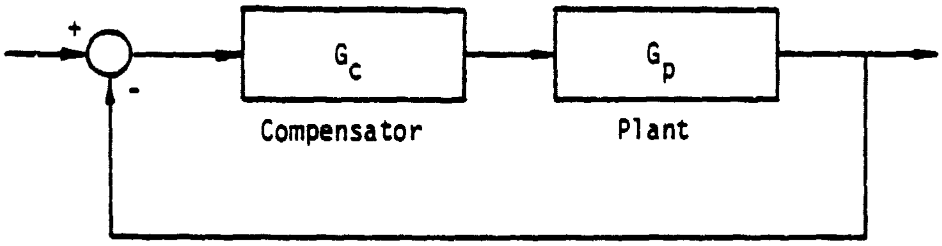

(a) Series compensation

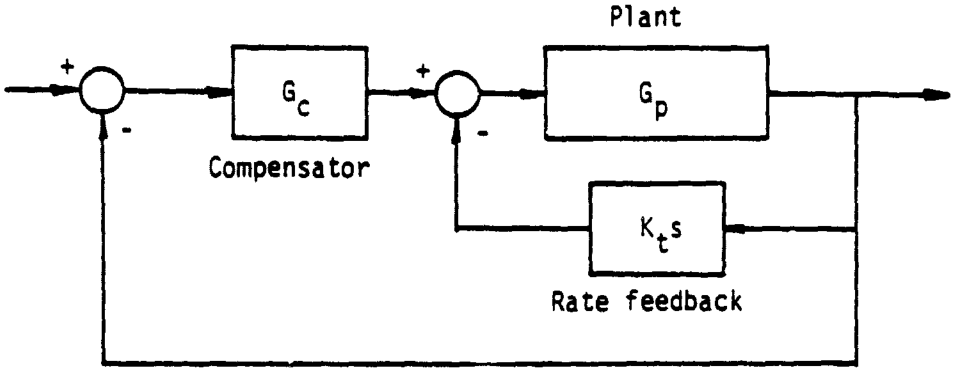

(b) Series compensation with rate feedback

Figure 27. Compensation schemes.

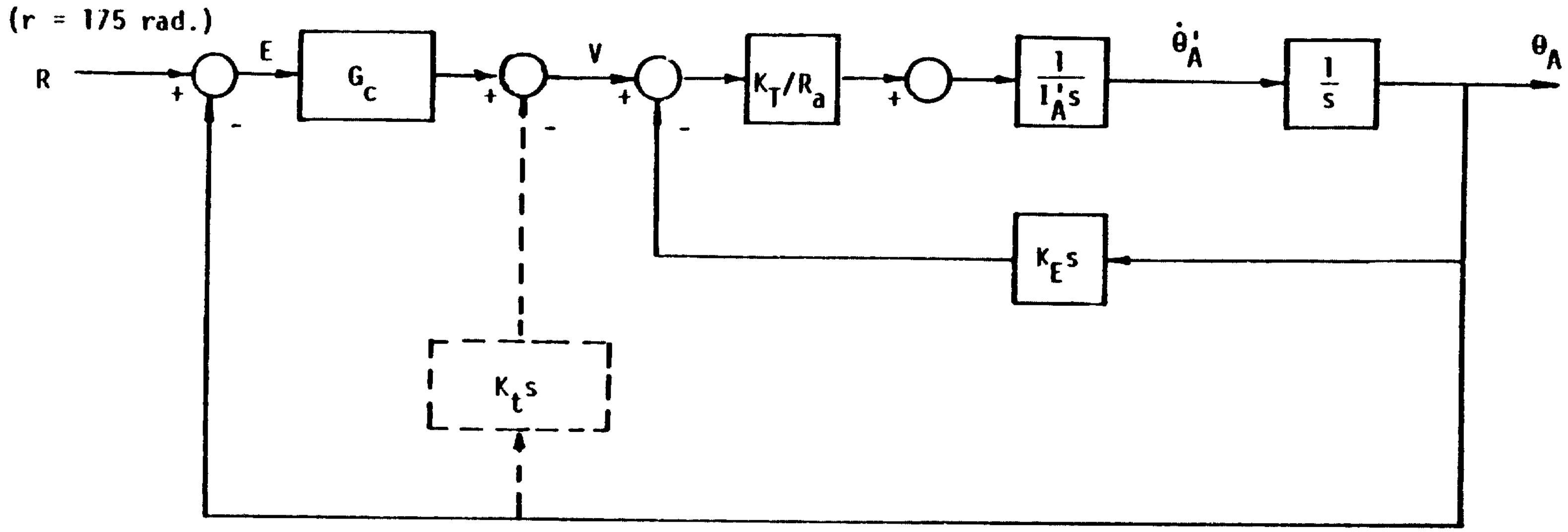

Figure 28. Closed-loop control system simulation diagram.

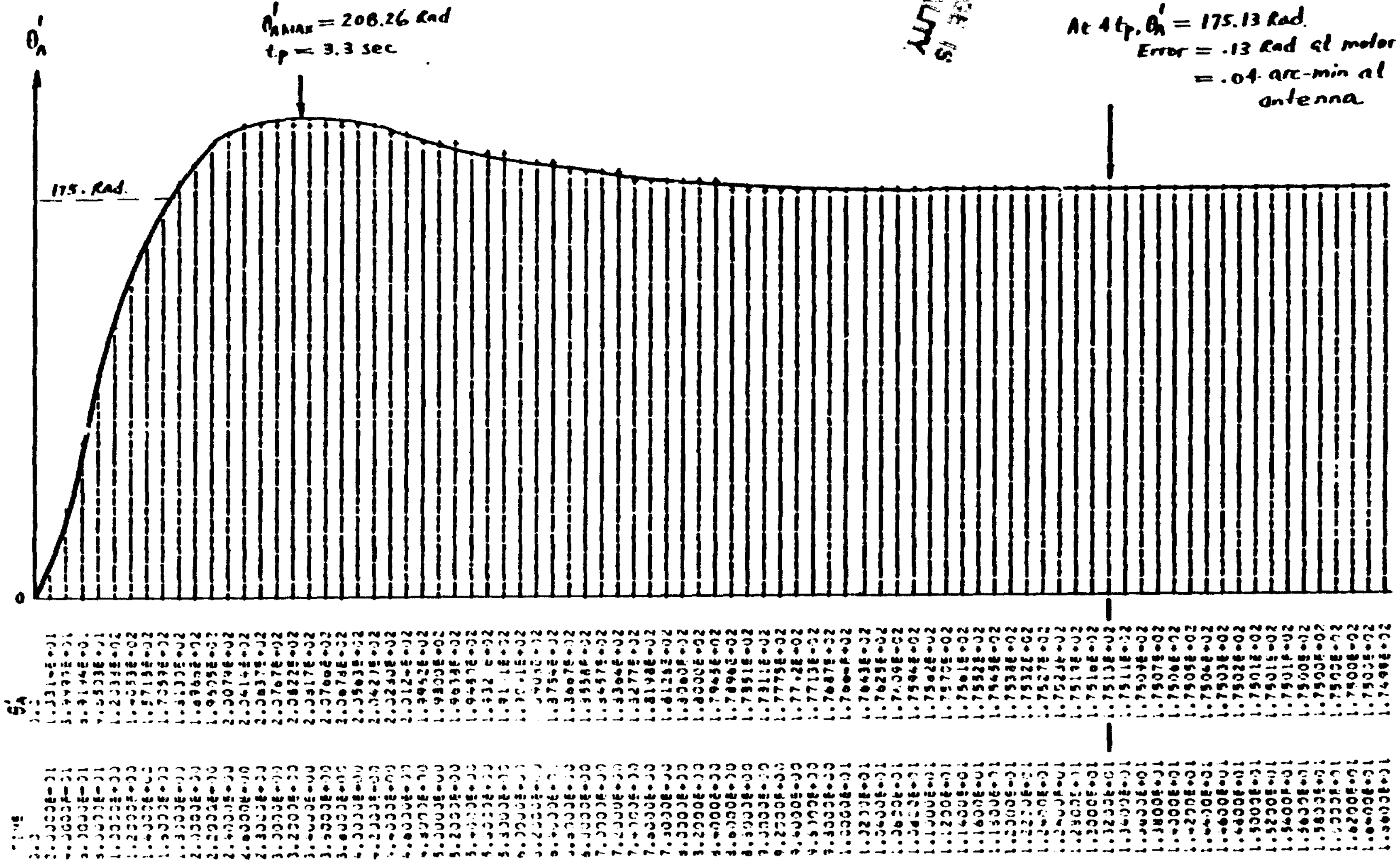

Figure 29. Step response of the nominal system.

of the system under the nominal conditions. The reference input is 175 radians for motor, corresponding to 1° for the antenna. It should be mentioned that the system is not expected to be subjected to a step function type of command. Step response simulation is used merely to reveal the system's transient characteristics.

System Sensitivity The response sensitivity of the designed system was studied by way of computer simulation. Results are given in Table 3. As a whole, the response did not change much for parameter change as high as 20%. Also, the superiority of the series compensation with rate feedback is evident.

The Constant Drag Torque Since the first rotary joint does not change its direction of rotation the nonlinear slip-ring friction torque appears as a constant drag torque with a magnitude of τ_{max} entering the system at the point as shown in Figure 30. Results of a step response simulation are given in Table 4. One sees that the control is capable of nulling the effect of constant drag torque very effectively. A CSMP listing of the simulation is attached as Appendix A.

Table 4. Response of System with Drig Friciton

Overshoot η		21%
Time to peak t_p		3.3 sec
Error at 4 t_p:	motor angle	.13 rad
	antenna angle	.04 arc-min

Theoretically, the steady-state pointing error due to a constant drag torque should be zero. From Figure 30, the response of the system output due to a constant disturbance torque $\tau_F = \frac{A}{s}$ is

Table. 3. System Sensitivity.

	System condition	Overshoot η	Time to peak t_p	Settling time t_s
Series compensation	Nominal	19 %	3.4 s	9.0 s
	K_T/R_a 10 % up	16 %	3.2 s	9.6 s
	" 10 % down	21 %	3.6 s	8.8 s
	" 20 % up	15 %	3.2 s	9.8 s
	" 20 % down	24 %	3.8 s	8.6 s
Series compensation with rate feedback	Nominal	19 %	3.2 s	8.8 s
	" 10 % up	19 %	3.2 s	8.8 s
	" 10 % down	20 %	3.2 s	8.8 s
	" 20 % up	18 %	3.2 s	8.8 s
	" 20 % down	20 %	3.2 s	8.6 s

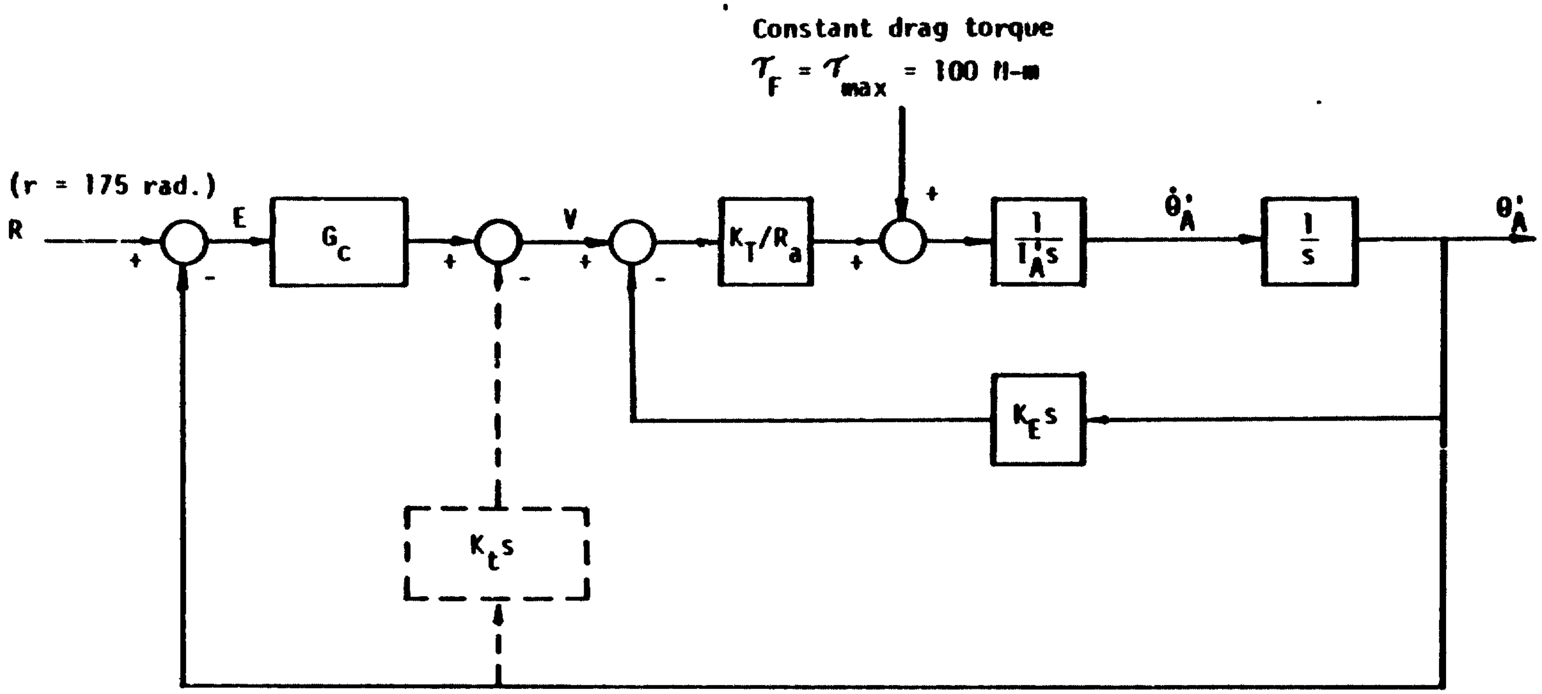

Figure 30. System with constant drag torque.

$$\theta_A'(s) = \frac{1}{I_A' s^2 + \frac{K_T}{R_a}[G_c(s) + K_E(1 + \beta)s]} \frac{A}{s} \tag{79}$$

The steady-state value of θ_A' is

$$\theta_A' (t \to \infty) = s\theta_A'(s \to 0) = 0 \tag{80}$$

where the property $G_c(s \to 0) = \infty$ has been used.

The Nonlinear Friction Torque The second rotary joint has little rotation under the nominal conditions. To counter anamalous effects, it may rotate in either direction. Thus the shifting hysteresis type of nonlinear friction torque, as portrayed in Figure 17, may come into play. This friction torque is a nonlinear function of the speed of the motor, and it enters the system in a way as shown in Figure 31. The nonlinear function is designated G_F. G_F can be simulated according to the flow diagram of Figure 19. Note that all load quantities have been reflected into quantities as seen by the motor; the value for K_F in Figure 19 should be handled similarly. Using the data in Figure 17,

$$K_F = -10^6 \frac{\text{N-M}}{\text{Deg}} \quad \text{at antenna}$$

$$= - \frac{\frac{57.3\text{x}10^6}{10^4} \text{ N-M}}{10^4 \quad \text{rad}} = -.573 \frac{\text{N-M}}{\text{rad}} \quad \text{at motor}$$

$$\tau_{max} = 10^6 \text{ N-M} \quad \text{at antenna}$$

$$= \frac{10^6}{10^4} = 100 \text{ N-M} \quad \text{at motor}$$

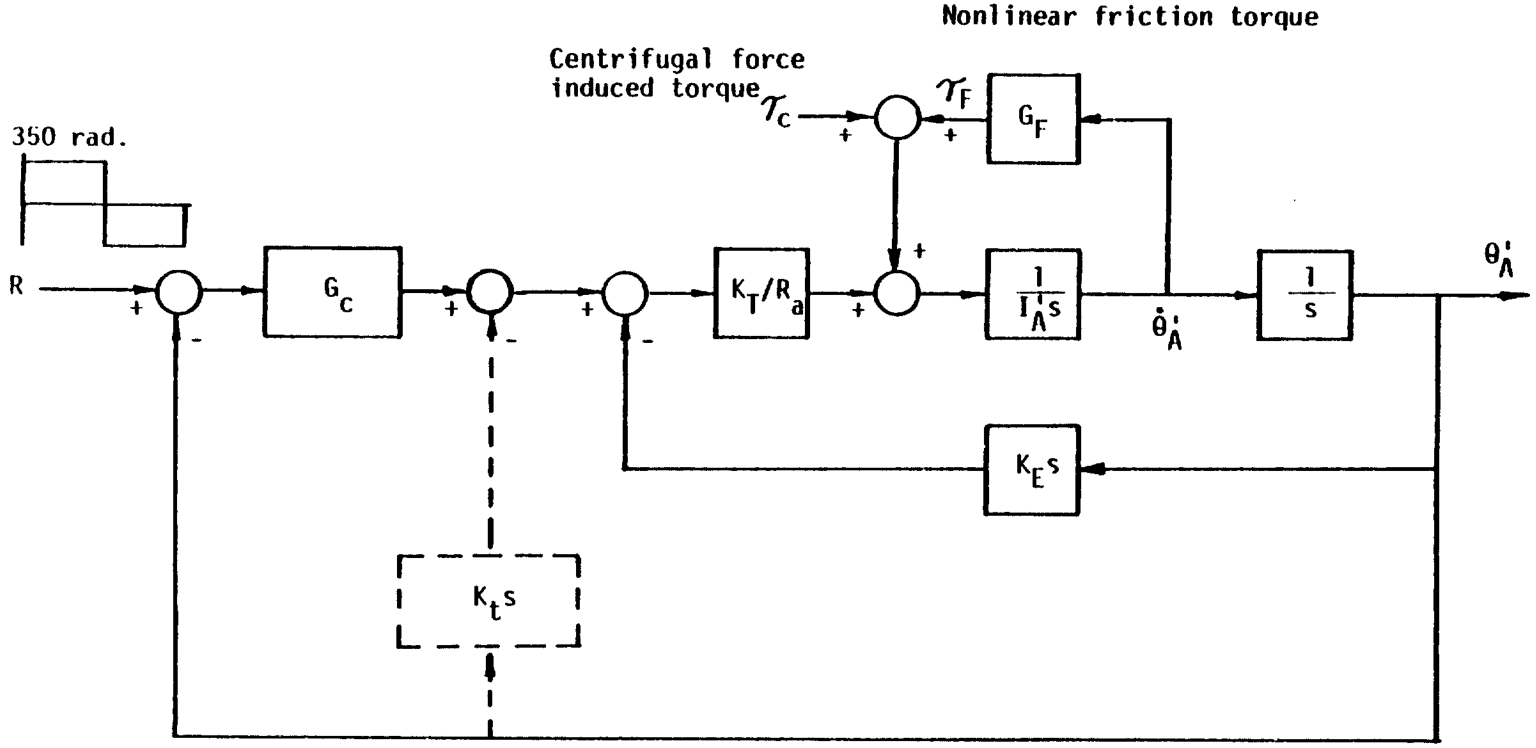

Figure 31. System with nonlinear friction torque.

To reveal the effect of nonlinear friction torque, a square-wave may be used as reference input for system simulation since rate reversal is needed to exhibit the shifting hysteresis characteristic of the nonlinearity. In order to drive the nonlinear friction torque to its saturation level the amplitude of the square-wave should be greater than 1° in terms of the actual antenna angle. An amplitude of 2° is chosen. The corresponding amplitude for the motor angle is $(2 \times 10^4)/57.3 = 349.04$ radians. A simulation was performed in the manner described. Results of simulation are listed in Table 5, which shows the adequancy of the control. Appendix B contains the CSMP listing of the simulation.

Table 5. Square-Wave Response of the System having Shifting Hysteresis Type of Friction Torque

Overshoot η		20%
Time to peak t_p		3.19 sec
Error at 4 t_p:	Motor angle	.14 rad
	Antenna angle	.05 arc-min

The Centrifugal Force Induced Torque τ_c Recall from the discussion in Section 3.4 that the maximum torque on antenna caused by the centrifugal force is less than .3% of τ_{max} which is 100 N-M as seen by the motor. Insert $\tau_c = 1$ N-M, which is 1% of τ_{max}, into the last simulation program and repeat the simulation. The results are nearly the same as those in Table 5, showing that the pointing control is capable of nulling the effect of τ_c satisfactorily.

3.8 Effect of Noise in Sensed Pointing Error Signal

It has been shown that, based on the set of given assumptions, the designed mechanical pointing control system more than adequately meets the 3-arc-minute requirement for pointing accuracy. If the microwave sensed pointing error is noise contaminated, however, the situation could be quite different. As discussed in Section 2, the noise in sensed error is low frequency in nature, which can be as low as d-c. Under this condition the noise directly dictates the accuracy of the overall pointing control system. At this moment, it is not practical to arrive at a numerical value for the noise level. The remark here serves to emphasize the possible adverse effect of the noise.

3.9 Effect of Collector Vibrations

It has been discussed in Section 3.7 that the frequencies of vibration for the collector is less than .001 hertz which is considerably lower than .2 hertz, the approximate bandwidth of the pointing control system. Therefore one expects errors caused by the collector vibration be effectively diminished by the pointing control. To support this claim, computer simulations were performed as follows.

Pointing error caused by collector vibration is equivalent to the error of the closed-loop control system excited by a sinusoidal reference input. Reference inputs having frequencies of .001 hertz (about 16.6 minute/cycle) and .01 hertz (about 1.66 minutes/cycle) were used in the simulations. Results are shown in Table 6, which confirm the claim.

Table 6. Tracking Error Due to Collector Vibrations

First simulation

vibration frequency = .001 hertz (≈ 16.6 min/cycle)

vibration amplitude = 1 degree

maximum steady-state error = .0055 rad. at motor

.002 arc-min at antenna

Second simulation

vibration frequency = .01 hertz (≈ 1.66 min/cycle)

vibration amplitude = 1 degree

maximum steady-state error = .55 rad. at motor

.19 arc-min at antenna

4. APPROACHES FOR MODELING THE FLEXIBLE COLLECTOR BODY

It is recognized that the structural dynamics of the flexible collector body may be modeled by transforming it to an equivalent orthotropic plate. Then the wealth of well known theory of plates can be applied readily. However, a thorough study of the structural responses of the collector plate requires a major effort. The discussion here will focus on the two approaches which may be used to obtain the desired model. They are the analytical approach and the simulation approach.

The Analytical Approach In this approach the structure of the collector truss is first transformed to an equivalent grid, which is then transformed to an equivalent orthotropic plate as shown in Figure 32. The differential equation for an orthotropic plate, including the inertial-force term, has the form [5]

$$D_x \frac{\partial^4 \omega}{\partial x^4} + 2H \frac{\partial^4 \omega}{\partial x^2 \partial y^2} + D_y \frac{\partial^4 \omega}{\partial y^4} = q + \rho h \frac{\partial^2 \omega}{\partial t^2} \tag{81}$$

where $\omega = \omega(x,y,t)$ is the deflection in the z-direction as shown in Figure 32(c), q is the external loading per unit area, h is the thickness, and ρ is the density of the plate material. The problem of modeling, simply stated, is the determination of constants D_x, D_y, and H.

Transformation from grid work to an orthotropic plate has been thoroughly studied by Timoshenko and his cohort [1]. Let the geometry of a grid be defined in Figure 33, then the constants for an equivalent orthotropic plate are given by

$$D_x = \frac{E\,h^3}{12} \quad \frac{t_1}{b_1}$$

$$D_y = \frac{E\,h^3}{12} \quad \frac{t_2}{a_1}$$

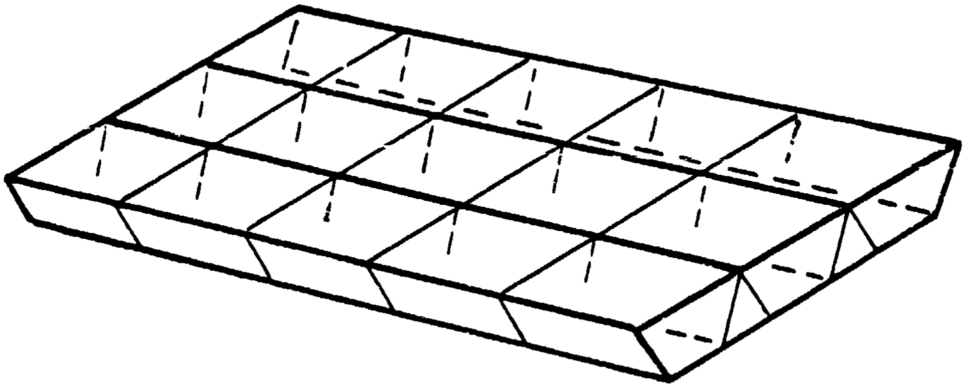

(a) The collector truss

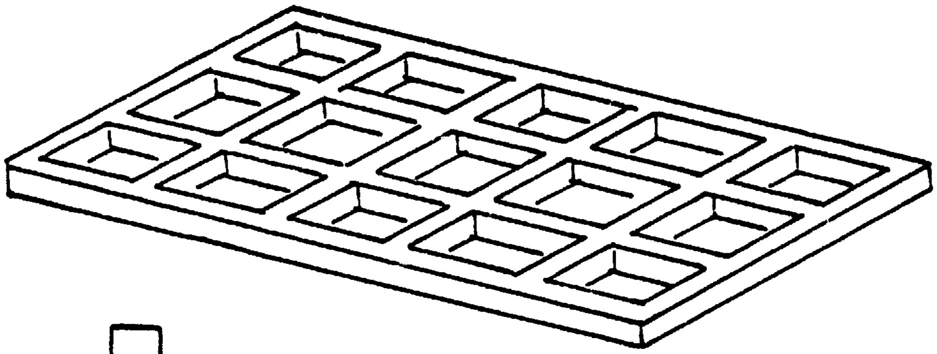

(b) An equivalent grid

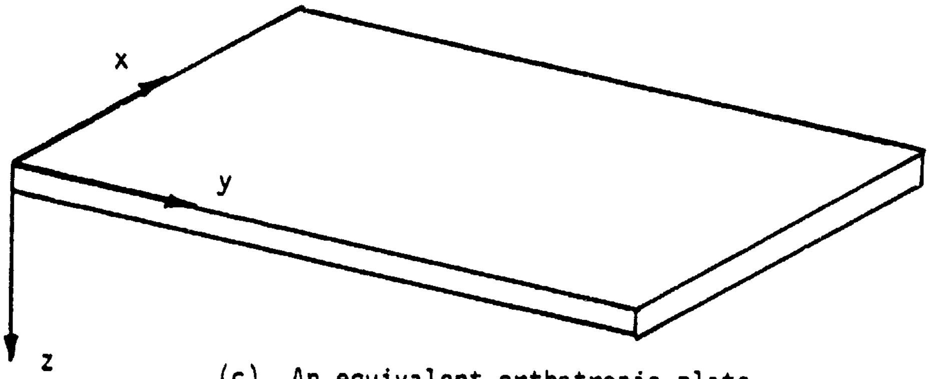

(c) An equivalent orthotropic plate

Figure 32. Transformation to an equivalent orthotropic plate.

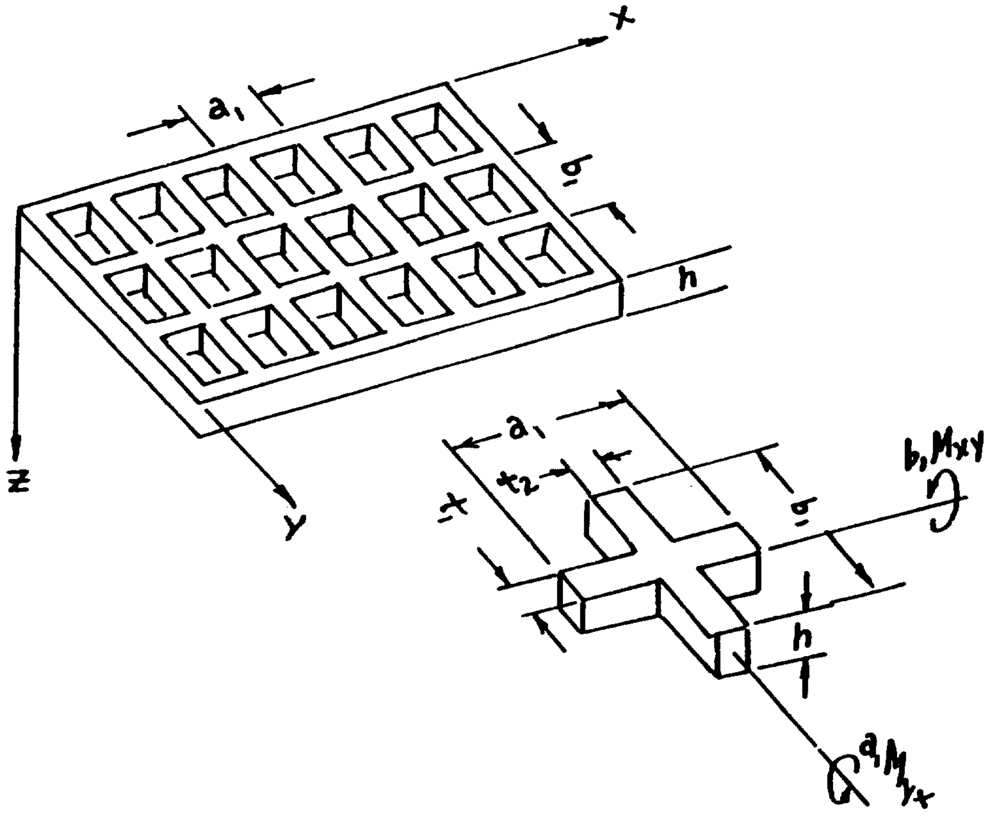

Figure 33. Definition of the geometry of a grid.

$$H = \frac{1}{2}\left(\frac{c_1}{b_1} + \frac{c_2}{b_2}\right) \tag{82}$$

where E is the modulus of elasticity, and c_1 and c_2 are torsional rigidities of the beams parallel to the x and y axes, respectively. When the beams have rectangular cross-section as shown, c_1 and c_2 are given by [6]

$$c_1 = \frac{G}{3} t_1^3 h[1 - \frac{192}{\pi^5} \frac{t_1}{h} \sum_{n=1,3,5---}^{\infty} \frac{1}{n^5} \tanh\left(\frac{n\pi}{2} \frac{h}{t_1}\right)$$

$$c_2 = \frac{G}{3} t_2^3 h[1 - \frac{192}{\pi^5} \frac{t_2}{h} \sum_{\substack{n=1,3,\\5,---}}^{\infty} \frac{1}{n^5} \tanh\left(\frac{n\pi}{2} \frac{h}{t_2}\right)] \tag{83}$$

For most practical cases the infinite series converges rapidly; usually two or three terms are sufficient to give accurate result. For example, if $\frac{h}{t_1} = 1$, then

$$\sum_{n=1,3,5---}^{\infty} \frac{1}{h^5} \tanh \frac{n\pi}{2}$$

$$= \tanh\frac{\pi}{2} + \frac{1}{3^5} \tanh\frac{3\pi}{2} + \frac{1}{5^5} \tanh\frac{5\pi}{2} + - - -$$

$$= 0.91715 + \frac{1}{243}(0.9998) + \frac{1}{3125}(1) + - - -$$

$$= 0.91715(1 + .004486 + .0003489 + - - -)$$

$$= 0.9216$$

Similarly, the results of the series become 1.00073 and 1.00414 for $\frac{h}{t_1}$ equals 2 and 4 respectively. Using the result for $\frac{h}{t_1} = 2$ in (83) gives

$$c_1 = \frac{G}{3} t_1^3 h[1 - \frac{192}{\pi^5} (\frac{1}{2}) (1.00073)]$$

$$= \frac{G}{3} (\frac{t_1}{h})^3 h^4 (0.6861)$$

$$= \frac{G}{3} (\frac{1}{8}) h^4 (0.6861)$$

$$= 0.0286 G h^4$$

Clearly $c_2 = c_1$ if $t_2 = t_1$. The bending moments and twisting moments are related to the deflection ω by the following expressions.

$$\begin{aligned} M_x &= - \frac{Eh^3}{12} \frac{t_1}{b_1} \frac{\partial^2 \omega}{\partial x^2} \\ M_y &= - \frac{Eh^3}{12} \frac{t_2}{a_1} \frac{\partial^2 \omega}{\partial y^2} \\ M_{xy} &= \frac{c_1}{b_1} \frac{\partial^2 \omega}{\partial x \partial y} \\ M_{yx} &= \frac{c_2}{a_1} \frac{\partial^2 \omega}{\partial x \partial y} \end{aligned} \qquad (84)$$

Analytic methods for transforming a truss structure as shown in Figure 32(a) to an equivalent grid, or directly to an equivalent orthotropic plate have not been developed. It is this part of the study which requires a major effort. However, some related cases have been studied, such as plates with many holes [7-10] and corrugated pipes. [7-11]. The equivalent solid plate or smooth pipe will produce the same strain, deformation, or strain energy as the actual perforated plate or corrugated pipe. The results for the actual structure have been carried out by testing, numerical calculation through point-matching or collocation technique, and other appropriate analysis such as energy method.

The Simulation Approach Constant D_x, D_y, and H of Eq. (80) for a given truss may be obtained by a parameter matching technique with the help of computer simulation. Well known computer programs exist, such as NASTRAN and STRDYN, which use finite element approximations for flexible structure.

5. CONCLUSION

A study of the pointing control system for SPS was accomplished. The study included two major areas, namely, the analysis of a pointing error sensing method for the SPS antenna, and the design of a mechanical pointing control system for the antenna. In addition, approaches for modeling the flexible body collector dynamics were given.

In the area of point error sensing, an analysis was made on a previously proposed method for developing pointing angle signals to be used by a servomechanism to point the antenna toward a rectenna on ground. From the analysis result, the method was found to be feasible. A normalized technique was added to the method to produce error signals that are independent of the received signal magnitude. Effects of vibration and noise on pointing control accuracy were analyzed and presented in the form of charts.

In the area of mechanical pointing control of the antenna, a baseline satellite configuration was selected as shown in Figure 16 (p. 30) together with a set of baseline parameters. Analysis were made on various phenomena which might influence the accuracy of the pointing control. They include the nonlinear slip-ring friction of rotary joints, motor characteristics, effect of centrifugal force induced torque, effect of variation in antenna's moment of inertia, effect of finite collector mass on pointing control, and the effect of vibration modes of the collector. The friction and backlash characteristics of the gear train was not available for analysis and were ignored. A mathematical model of the plant, whose output is the antenna pointing direction, was developed. The pointing control system was designed using an optimal control approach with the help of the root-square-locus method.

The mechanical pointing accuracy, with the various anomalies present, was found to be well within 1 arc-minute.

From the results of this study it appears that the desired pointing accuracy of ± 3 min is possible. Suppose a reasonable error budget is ± 1 min for each of the major error sources of (1) noise, (2) vibration, and (3) mechanical effects (gear backlash, stricktion, etc.). Suppose further that we require the ± 3 min to correspond to at most 50% of the beamwidth θ_B so that operation is always in the linear part of the error pattern. Then from Figure 13 and $\theta_B = 12$ min we require $M \leq 3$ subarrays in the linear array. The allowed vibration error is therefore 1 min/12 min = 0.083 or 8.3% of θ_B maximum. From Figure 12 this allowance is not exceeded for $M=3$ even for mode 2 ($k=2$) vibration ($\overline{\Delta z} = 1$ m). The noise error of ± 1 min can be achieved by providing sufficient power in the ground station pilot transmitter.

6. REFERENCES

[1] Hung, J.C. and P.Z. Peebles, Jr., "Final Report, Accuracy Analysis of Pointing Control System of Solar Power Station," NASA Contract NAS8-33065 with the Electrical Engineering Department, University of Tennessee, December 23, 1978.

[2] Peebles, Peyton Z., Jr., Probability, Random Variables, and Random Signal Principles, McGraw-Hill Book Co., 1980.

[3] "Satellite Power Systems (SPS) Concept Definition Study", Final Report, Vol. 3, SD-78-AP-0023-3, Rockwell International, Space Division, April 1978, p. 3-201.

[4] Chang, S.S.L., Synthesis of Optimum Control Systems, McGraw-Hill Book Co., 1961.

[5] Timoshenko, S., and S. Woinowsky - Krieger, Theory of Plates and Shells, second edition, McGraw-Hill Book Co., 1959.

[6] Timoshenko, S., and Goodier, Theory of Elasticity, Thrid edition, McGraw-Hill Book Co., 1970.

[7] Goldberg, J.E., and K.N. Jabbour, "Stresses and Displacements in Perforated Plates," Nuclear Structural Engineering, Vol. 2, pp. 360-381., 1965.

[8] Hulbert, L.E., and F.W. Niedenfuhr, "Accurate Calculation of Stress Distributions in Multiholed Plates," J. Eng. for Ind. Trans. ASME, Vol. 87, pp. 331-343, 1965.

[9] Meijers, P., "Doubly-Periodic Stress Distributions in Perforated Plates," Ph.D. Thesis, Technological University of Delft, the Netherlands, 1967.

[10] Slot, T., and W.J. O'Donnell, "Effective Elastic Constants for Thick Perforated Plates with Square and Triangular Penetration Patterns," J. Eng. for Ind., Trans. ASME, Vol. 93, pp. 935-942, 1971.

[11] Donnell, L.H., "The Flexibility of Corrugated Pipes Under Longitudiual Forces and Bending," Trans. ASME, Vol. 54, pp. 69-75.

APPENDIX A. CSMP FOR THE FIRST ROTARY JOINT CONTROL SYSTEM.

```
                ****CONTINUOUS SYSTEM MODELING PROGRAM****

          ***PROBLEM INPUT STATEMENTS***

*         STEP RESPONSE WITH DRAG DISTURBANCE
          R=175.
          TD=100.0
          E=R-C
          X1=13.75*E
          X2=INTGRL(0.0,X1)
          X3=LEDLAG(3.164,0.193,X2)
          X4=DERIV(0.0,X3)
          X9=2.36*X4
          V=X9+X3
          E3=V-C2
          C2=43.4*C1
          C1=DERIV(0.0,C)
          C2=43.4*C1
          X5=96.05*E3
          X6=TD+X5
          X7=0.00010173*X6
          X8=INTGRL(0.0,X7)
          C=INTGRL(0.0,X8)
*
TIMER  FINTIM=20., OUTDEL=.2, DELT=.001, PRDEL=.2
PRTPLT E, V, C
LABEL  STEP RESPONSE WITH DRAG DISTURBANCE
END
STOP
```

APPENDIX B. CSMP FOR THE SECOND ROTARY JOINT CONTROL SYSTEM.

```
                ****CONTINUOUS SYSTEM MODELING PROGRAM****

          ***PROBLEM INPUT STATEMENTS***

*      POINTING CONTROL WITH SHIFTING HYSTERESIS TYPE
*      OF NONLINEAR FRICTION TORQUE
*      KF=-.573, DELT=.001, D=KF*DELT
INITIAL
       CONSTANT SGNP=0.,TM=100.,TDP=0.,TD=0.,D=-.000573
DYNAMIC
   SORT
       R=350.*STEP(0.0)-200.*STEP(10.0)
       E=R-C
       X1=25.18*E
       X2=INTGRL(0.0,X1)
       X3=LEDLAG(2.20,0.270,X2)
       X4=DERIV(0.0,X3)
       X9=2.36*X4
       V=X9+X3
       E3=V-C2
       C2=43.4*C1
       C1=DERIV(0.0,C)
       C2=43.4*C1
       X5=96.05*E3
       X6=TD+X5
       X7=0.00010173*X6
       RATE=INTGRL(0.0,X7)
       C=INTGRL(0.0,RATE)
   NOSORT
       SGN=SIGN(1.0,RATE)
       IF (SGN .EQ. SGNP) GOTO 301
       TDP=0.
  302  TD=TDP+D*RATE
       IF (ABS(TD) .GT. TM) TD=SIGN(TM,TD)
       GO TO 304
  301  IF (ABS(TDP) .EQ. TM) GOTO 303
       GOTO 302
  303  TD=TDP
  304  TDP=TD
       SGNP=SGN
   SORT
*
TERMINAL
TIMER  FINTIM=20., OUTDEL=.2, DELT=.001, PRDEL=.2
         METHOD RKSFX
PRTPLT C, E, RATE, TD
LABEL  STEP RESPONSE
END
STOP
```